SPE-215083-MS

An Analytical Tool to Predict Fracture Extension and Elastic Desaturation for Polymer Field Projects

M. B. Abdullah, University of Texas at Austin, Austin, TX, USA / Kuwait University, Kuwait; R. S. Seright, New Mexico Institute of Mining & Technology, Socorro, NM, USA; M. V. B. Machado, PETROBRAS; M. Delshad and K. Sepehrnoori, University of Texas at Austin, Austin, TX, USA

This paper was prepared for presentation at the 2023 SPE Annual Technical Conference and Exhibition held in San Antonio, Texas, USA, 16 - 18 October 2023.

Abstract

Induced fractures often play a key role in achieving acceptable injectivity during polymer floods, especially for vertical injection wells. However, fracture extension must be controlled to prevent severe channeling between the wells and compromise the flood performance. This paper presents a physics-based analytical model to predict polymer injectivity and fracture length as a function of polymer rheology, injection rate, and reservoir geomechanical properties. The analytical injectivity model is based on the unified viscoelastic model by Delshad et al. (2008). The injectivity model is coupled with 2-D fracture models: Perkins-Kern-Nordgren (PKN) and Kristianovich-Geertsma- de Klerk (KGD). In addition, the model is coupled with the elastic desaturation curve to predict additional oil recovery due to polymer viscoelasticity as a function of the leak-off rate through the fracture faces. Finally, a sensitivity study is conducted on reservoir properties and polymer rheology to understand the dominant factors that control fracture extension.

The analytical model shows good agreement in injectivity and fracture length with two other fracture numerical simulation models (Gadde and Sharma 2001, Ma and McClure 2017). The degree of fracture extension is a strong function of formation permeability, with relatively short fractures predicted for the high permeability characteristics of most commercial-scale polymer floods. We also examine conditions when relatively high leak-off rates through fracture faces might allow the viscoelastic nature of HPAM solutions to displace capillary-trapped residual oil. This is the first analytical solution for coupled polymer injectivity and fracture-length based on real HPAM rheology that can be used by a simple mathematical software or Excel worksheet. The developed tool can assist field operators in reducing the uncertainty and risk in polymer injectivity and quantifying fracture extension in the reservoir.

Keywords: Polymer, EOR, Viscoelasticity, Fracturing, Injectivity

Introduction

Polymer flooding is the most widely employed and developed chemical enhanced oil recovery (EOR) technique. The primary objective of polymer flooding is to improve sweep efficiency by increasing the viscosity of the injectant aqueous phase (Sorbie 1990). Various polymer lab studies, field pilots, and full-field projects have been conducted since the 1950s (Standnes and Skjevrak 2014). Recent advances in polymer flooding extended the polymer applicability to harsh reservoir conditions over 70 °C and 100,000 ppm of TDS (Dupuis et al. 2017, Al-Murayri et al. 2019, Seright et al. 2021, Skauge et al. 2022, Hassan et al. 2022). Synthetic polymers, such as hydrolyzed polyacrylamide polymers (HPAM), are the most common polymers utilized in EOR. This is because they are more readily available and have better cost viability than biopolymers like xanthan gum for field-scale operations (Sheng 2013).

Polymers are non-Newtonian fluids that exhibit shear-thinning behavior when the shear rate increases. HPAM polymers are known for their viscoelastic behavior in porous media. HPAM with higher-molecular weights and concentrations exhibits higher viscoelasticity (Qi et al. 2017, Erincik et al. 2018). Viscoelasticity is a time-dependent phenomenon in which polymers relax and contract as they move through porous media. If the polymer relaxation time exceeds the residence time, the coiled polymer chains do not have sufficient time to disentangle, and polymer viscosity increases (shear-thicken). Residence time is inversely proportional to the shear rate or fluid velocity (Azad 2022). Often, polymer viscoelasticity is represented by the ratio between polymer relaxation time and residence time, known as Deborah number (N_{De}) (Delshad et al. 2008, Qi et al. 2017).

Shear thickening or elongational viscoelastic behavior is expected around the injector vicinity, at which maximum velocity is observed (Seright 1983, Delshad et al. 2008, Glasbergen et al. 2015, Seright et al. 2023). Such behavior can significantly decrease injectivity as the aqueous phase viscosity increases (Wang et al. 2008, Seright et al. 2009). On the contrary, some field projects recorded enhancements in injectivity (Clemens et al. 2013, Manichand et al. 2013, Melo et al. 2017, Dandekar et al. 2021). This finding is explained by developing fractures around the wellbore when the fluid viscosity increases injection pressure above the reservoir parting pressure (Seright et al. 2009, Zechner et al. 2015, Seright 2017, Hwang et al. 2019, Shankar and Sharma 2022). However, fracture propagation from the injector to the producer and over one-third of the distance between the wells may reduce sweep efficiency (Dyes et al. 1958, Seright 2017).

There are different attempts in the literature to develop models to predict fracture extension due to polymer viscoelasticity. For example, Gadde and Sharma (2001) developed the University of Texas Well Injectivity Decline simulator (UTWID), which is a single-well numerical simulator to predict fracture geometry for water flooding. The model accounts for practical plugging, changes in thermal stresses, and the impact of changes in pore pressure (Suri and Sharma 2009, Suri et al. 2011). UTWID is based on PKN fracture model (Nordgren 1972). Later, UTWID was enhanced to predict fractures induced by viscoelastic polymers (Lee 2012, Zechner et al. 2015, Hwang et al. 2019, Hwang et al. 2022). Seright et al. (2009) presented a simplified analytical model that predicts fracture length based on polymer filterability tests in the lab. As more polymer is injected, the filter-cake resistance factor increases, which increases fracture extension in vertical wells. Li et al. (2016) coupled a two-dimensional (2-D) KGD fracture model (Geertsma and De Klerk 1969) with the mechanistic chemical flooding reservoir simulator developed at The University of Texas at Austin (UTCHEM). Polymer rheology was modeled using the unified viscoelastic model (UVM) (Delshad et al. 2008). Their model accounts for fracture propagation by enhancing cells' matrix permeability along the fracture length in the reservoir simulator and using a 5-spot pattern with corner producers to maintain a constant boundary pressure. Ma and McClure (2017) developed a single-phase 2-D discrete fracture network simulator, which couples fluid flow with stress variation during fracturing (Complex Fracturing Research Code or CFRC). The model assumes that prior to polymer injection, water is injected until reaching a steady state pressure gradient with a constant boundary pressure. The UVM was used for polymer rheology in the matrix. The study mainly discussed the enhancement in injectivity as fractures are induced. Li et al. (2022) constructed a grain-scale model to predict fracture initiation and injectivity during polymer injection. They coupled computational fluid dynamics model with the discrete element method. The model incorporates the impact of water quality, undissolved polymer in water, and polymer viscoelastic rheology on injectivity. Enhancement in injectivity is found as fractures are initiated due to polymer shear-thickening. Unfortunately, the model is designed for a small scale (0.6 m from the wellbore) and is computationally expensive for large field scale models.

Another way to evaluate the fracture initialization and propagation during polymer injection is to couple reservoir flow and geomechanics with CMG-GEM commercial compositional reservoir simulator (CMG 2022). The coupling between the reservoir flow and geomechanics is an iterative method by which the pore pressure and deformation are solved separately and sequentially. The CMG-GEM simulator accounts for polymer viscoelasticity and assumes 2-D PKN or KGD fracture models. In this study, we apply the one-way coupling, where pressure is sent from the reservoir simulator to its geomechanics model to compute deformations, stresses, and strains. However, no information is sent back from the geomechanics model for flow calculations. Therefore, when the pressure in the reservoir changes due to fluid injection, stresses on gridblocks attached to the fracture will affect the fracture mechanism (Tran et al. 2008, Tran et al. 2013). The connection between those two generic neighbor gridblocks remains intact or breaks depending on the exerted tensile stress. When the exerted tensile strength on a gridblock is less than the rock tensile strength, the fracture is initiated and propagates through the gridblocks (Tran et al. 2012).

Recent studies suggested that polymer viscoelasticity could reduce residual oil saturation beyond waterflooding. During the flow of viscoelastic polymer through small pores, long polymer chains apply large forces on the trapped oil droplets, grab its upper part, and as a result, detach oil droplets from dead-end pore surfaces (Wang et al. 2010, Mirzaie Yegane et al. 2022). Corefloods demonstrated a reduction in waterflood residual oil up to 5% OOIP with viscoelastic polymers, post-injecting large volumes of water or viscous-glycerin flood (Erincik et al. 2018, Koh et al. 2018, Jin et al. 2020). Lotfollahi et al. (2016) presented an empirical correlation between elastic oil desaturation and trapping number. Qi et al. (2018) proposed an elastic desaturation curve (EDC) that correlated Deborah number to residual oil-saturation reduction based on coreflood experiments of HPAM-Flopam-3630S (SNF-FLORGER 2012). Azad and Trivedi (2021) suggested another elastics desaturation curve based on extensional polymer viscosity measurement using a capillary break-up extensional rheometer. A recent study by Mohamed et al. (2023) presented an elastic desaturation curve based on micro-core two-phase injection. Among those studies, Qi et al. (2018) elastic desaturation curve is more convenient to apply and clearly differentiates the oil recovery resulting from polymer elasticity beyond water flooding. As such, we decided to implement their EDC in our study.

This study presents a physics-based analytical model to predict polymer injectivity and fracture length. Also, the anticipated additional oil recovery due to polymer viscoelasticity in the field is examined, even when the fracture is present. The analytical injectivity model is based on the unified viscoelastic model by Delshad et al. (2008). We coupled the injectivity model with 2-D fracture models of PKN and KGD. Then, we verified the polymer injectivity and fracture length against numerical models and a field study. Additionally, the model is coupled with the elastic desaturation curve to predict increased oil recovery owing to polymer viscoelasticity (Qi et al. 2018) as a function of flow through the fracture walls. Finally, a sensitivity study is conducted on reservoir properties and polymer rheology to highlight the dominant factors that can significantly control fracture extension.

Methodology

Polymer Rheology in Porous Media.

The unified viscosity model by Delshad et al. (2008) is widely used to model apparent polymer viscosity as the sum of shear and elongational viscosity (Kim et al. 2010, Lotfollahi et al. 2015, Ma and McClure 2017, Azad and Trivedi 2019a, Zeynalli et al. 2021, Alzaabi et al. 2020, Hwang et al. 2022):

$$\mu_{\text{app}} = \mu_{\infty} + \left(\mu_p^0 - \mu_w\right)\left[1 + (\lambda\dot{\gamma}_{\text{eff}})^2\right]^{\frac{n-1}{2}} + \mu_{\max}\left[1 - \exp\left(-\left(\lambda_2\tau\dot{\gamma}_{\text{eff}}\right)^{n_2-1}\right)\right], \tag{1}$$

where μ_∞ (cp) is the polymer viscosity at high shear rates that is assumed equivalent to water viscosity, μp0 (cp) is the polymer viscosity at low shear rates, μ_w (cp) is the water viscosity, μ_{max} (cp) is the maximum polymer viscosity in shear-thickening, n_2 is the exponent associated with the shear-thickening behavior, λ shear-thinning parameter (sec^{-1}), λ_2 shear-thickening parameter = 0.01 (unitless) (Zeynalli et al. 2022), and τ approximates insitu viscoelastic relaxation time (sec). The effective shear rate γ˙eff (sec^{-1}) in the reservoir is given by (Cannella et al. 1988).

Appendix A presents more details on how these parameters are calculated.

Polymer Rheology in Fracture.

Polymer rheology exhibits only shear thinning in fracture void space (Zechner et al. 2013). The shear thinning rheology in the fracture is commonly approximated using the simple power-law model (Vongvuthipornchai and Raghavan 1987, Suri and Sharma 2009, Zechner et al. 2015).

$$\mu_p = K\gamma^{n_p - 1}, \tag{2}$$

where, K and n_p are the power-law coefficient and exponent.

Unified Viscoelastic Injectivity Model (UVIM).

The injector wellbore bottomhole pressure (BHP) is calculated using UVIM, derived in our previous work (Abdullah et al. 2023). The model assumes that water is injected into the reservoir until reaching a steady-state and residual oil saturation, which is a reasonable assumption as most of polymer thickening behaviour is around the wellbore where oil is well-swept. Then the polymer is injected (Fig. 1). Throughout polymer injection, the BHP of the injection well increases while the outer boundary pressure (P_e) remains constant. Total pressure drop (ΔP_T) is the summation of the polymer pressure drop between the wellbore and the extent of the polymer slug (ΔP_p), calculated from UVIM, and water pressure drop (ΔP_w) from the polymer slug face to the reservoir boundary, calculated from Darcy's law.

$$\Delta P_T = \Delta P_p + \Delta P_w = BHP - P_e. \tag{3}$$

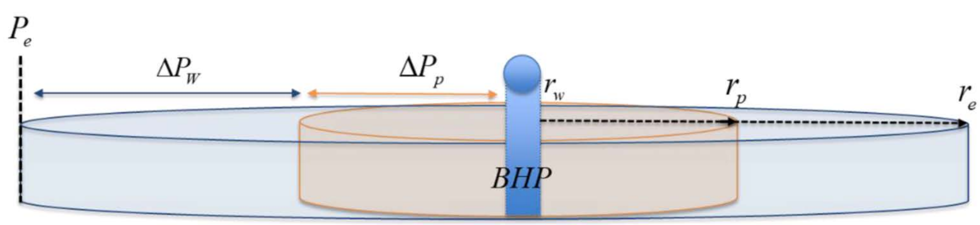

Figure 1—Schematic diagram of the UVIM conceptual reservoir model. The diagram illustrates the assumption that the reservoir is waterflooded (blue region) until reaching a steady-state and to the residual oil saturation, then the polymer is injected (orange region) (Abdullah et al. 2023).

ΔP_p is calculated by solving the following UVIM integral,

$$\Delta P_p = \int_{r_{we}}^{r_p} \frac{q}{2\pi r h k_p}\left(\mu_\infty + \left(\mu_p^0 - \mu_w\right)\left[1+\left(\lambda AB\left[\frac{q}{2\pi rh}\right]\right)^2\right] + \mu_{\max}\left[1-\exp\left(-\left(\lambda_2 \tau AB\left[\frac{q}{2\pi rh}\right]\right)^{n_2-1}\right)\right]\right) dr^{\frac{n-1}{2}}, \tag{4}$$

where the detailed explanation of the equation symbols are in **Appendix A.**

Solving the ΔP_p integral yields an initial value problem, which can only be analytically integrated using special functions theory and asymptotic methods. The obtained closed-form analytical solutions are represented in terms of Gauss hypergeometric functions, exponential integrals, and complementary incomplete gamma functions (Abramowitz et al. 1988, Andrew 1998). The detailed mathematical derivation is presented in our previous paper (Abdullah et al. 2023). For the pressure drop of water flooded zone, from the end of the polymer slug r_p to the reservoir boundary r_e, the Darcy equation is used in field units:

$$\Delta P_w = \frac{141q\mu_w}{kk_{rw}h}\ln\left(\frac{r_e}{r_p}\right). \tag{5}$$

Equivalent Wellbore Radius.

To account for fracture propagation as a result of polymer insitu rheology (i.e., elongational viscosity), we adopt the concept of "equivalent wellbore radius" (r_{we}) proposed by Prats (1961). Prats (1961) suggested representing the effect of fracture on well productivity by the r_{we}, in a pseudo-radial flow at a constant pressure at the boundary. In pseudoradial-flow, the fracture flux distribution is assumed stable, and the transient well behavior can be equated to an unfractured well with an enlarged wellbore radius (Economides and Nolte 2000, Friehauf et al. 2010, Miskimins 2019). The equivalent wellbore radius (Fig. 2) is given as

$$r_{we} = x_f r_{wD}, \tag{6}$$

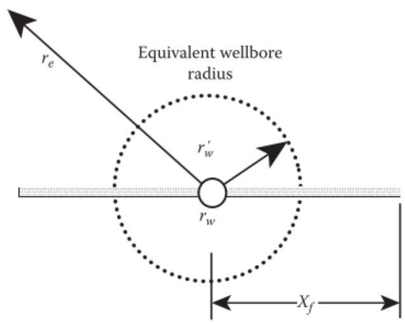

Figure 2—Equivalent wellbore radius conceptual model (Smith and Montgomery 2015).

where x_f is the distance from the wellbore to an arbitrary point along the fracture in ft, r_{wD} is dimensionless effective
wellbore radius that is correlated to the relative capacity parameter (a) as such rw,D=0.511+(a0.95)0.95,

$$a = \frac{\pi k x_f}{2k_f \bar{w}_f}. \tag{7}$$

The permeability (k_f) for unpropped fracture is calculated from the average fracture width as follows (Zhang 2019, Teng et al. 2020):

$$k_f = \frac{\beta \bar{w}_f^2}{12}, \tag{8}$$

where w¯f is the average fracture width in ft, β is a unit conversion from ft² to mD (9.413×10^{13}). By substituting Eq.(8) into Eq. (7), the relative capacity parameter (a) is calculated as

$$a = \frac{6\pi k x_f}{\beta \bar{w}_f^3}. \tag{9}$$

The relative capacity is related to fracture conductivity as $F_{CD} = \pi / 2a$. The fracture conductivity expresses the ratio between the ability of fracture to deliver fluid to the wellbore and the reservoir's ability to deliver fluid to the fracture. For infinitely conductive fracture, $F_{CD} > 10$ ($a < 0.16$) and the equivalent wellbore radius is $r_{we} \approx 0.5 \times x_f$ (Economides et al. 1994, Miskimins 2019).

Fracture Initiation and Closure Pressure.

As shown in Fig. 3, a fracture is initiated when the flowing bottomhole pressure of the injection well exceeds the fracture initiation or breakdown pressure (p_{fi}). p_{fi} is measured from a diagnostic fracture injection test (DFIT), or stress tests. Alternatively, it can be calculated as follows (Haimson and Fairhurst 1967, Economides and Nolte 2000):

$$p_{fi} = \frac{3\sigma_{h\min} - \sigma_{h\max} - 2\eta\Delta p_{res} + T_0}{2 - 2\eta}, \tag{10}$$

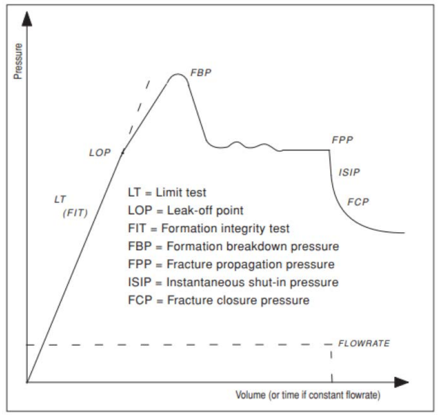

Figure 3—Schematic of mini-frac test for pressure versus volume of injection time. It illustrates that the fracture breakdown point is the highest pressure needed for fracture initiation. A propagation pressure is needed for fracture extension and a pressure higher than a closure pressure for the fracture to remain open (Zoback 2010).

where $\sigma_{h\ \min}$, $\sigma_{h\ \max}$, Δp_{res}, η, and T_0 are minimum horizontal stress, maximum horizontal stress, change in reservoir pressure, poroelastic constant (typically = 0.25 (Economides and Nolte 2000)), and tensile strength (we will discuss later), respectively. We assume a constant reservoir pressure, so that $\Delta p_{res} = 0$. The minimum horizontal stress is approximated as the fracture closure pressure (FCP), which can be estimated either from a fracture injection test or using rock properties as follows (Belyadi et al. 2019),

$$\sigma_{h\min} = \frac{v}{1-v}\left(\sigma_v - \alpha p_{res}\right) + \alpha p_{res}, \tag{11}$$

where v is Poisson's ratio, σ_v is vertical stress (is about 1 - 1.1 psi/ft in brine-saturated sandstone of 7-20% porosity, (Economides and Nolte 2000). p_{res} is pore or reservoir pressure, and α is Biot's poroelastic constant (Biot and Willis 2021) that is defined as α=1−cmcr, where c_m and c_r are rock and pore compressibilities in psi^{-1}. $\sigma_{h\ \max}$ is more challenging to measure than $\sigma_{h\ \min}$ and requires stress tests (Guo et al. 2017). When stress and fracture injectivity tests are not available, it is acceptable (Suri et al. 2011, Hwang and Sharma 2013, Zhang and Yin 2017, Hwang et al. 2019) to assume that,

$$p_{fi} = \sigma_{h\min}. \tag{12}$$

Fracture Propagation Criteria.

During fracture propagation, the maximum net pressure ($p_{net(\max)}$), which is calculated at the wellbore, is as follows (Economides and Nolte 2000, Sarvaramini and Garagash 2015),

$$p_{net(\max)} = \left(p_f - \sigma_{h\min}\right) = \frac{K_{IC}}{\sqrt{\pi A_f}}. \tag{13}$$

The right hand side term is known as fracture toughness or tensile strength term (Economides and Nolte 2000, Gadde and Sharma 2001). K_{IC} is the fracture toughness that is related to fracture surface energy (typically 500 - 2000 psi.inch$^{0.5}$(Gidley and Engineers 1989, Economides and Nolte 2000)), A_f is the fracture geometry parameter (if $2L_f > h_f$ then $A_f = h_f / 4$, or if $2L_f < h_f$ then $A_f = L_f$). Generally, the tensile strength term in Eq. (13) is small compared to $\sigma_{h\ \min}$ and can be neglected (Hwang and Sharma 2013). Zoback (2010) demonstrated that neglecting the tensile strength can decrease the fracture pressure at early fracture propagation, but this effect diminishes as the fracture extends. However, we will keep the fracture toughness term for model generality in the subsequent equations.

Gadde and Sharma (2001) suggested that the fracture will extend as long as the pressure at the fracture tip is larger than the fracture pressure at the wellbore. The propagation criterion mandates that,

$$p_{tip} > \frac{K_{IC}}{\sqrt{\pi A_f}} + \sigma_{h\min}, \tag{14}$$

where,

$$p_{tip} = BHP - p_{net(\max)}, \tag{15}$$

and,

$$p_{net(\max)} = p_f - \sigma_{h\min}, \tag{16}$$

where $p_{net(\max)} = p_f - \sigma_{h\,\min}$, then by substituting Eq. (15) in Eq.(14),

$$BHP - p_f + \sigma_{h\min} > \frac{K_{IC}}{\sqrt{\pi A_f}} + \sigma_{h\min}. \tag{17}$$

By re-arranging Eq. (17), the fracture propagation criteria shall satisfy the following condition:

$$BHP > \frac{K_{IC}}{\sqrt{\pi A_f}} + p_f. \tag{18}$$

Fracture Pressure and Geometry.
The fracture pressure will be calculated using a two-dimensional model for vertical fracture. Two popular fracture models are found in the literature with wide applications: PKN (Nordgren 1972) and KGD (Geertsma and De Klerk 1969) models (Fig. 4). Table 1 describes the key differences between the two models.

Table 1—Comparison between PKN and KGD models

Model	PKN	KDG
Fracture length to fracture height	$2L_f > h_f$ (Valko and Economides 1995)	$2L_f < h_f$ (Valko and Economides 1995)
Fracture height containment	Fixed, bounded within fracture layer (Valko and Economides 1995)	Fixed, relatively uncontrolled (Valko and Economides 1995)
Shape	Elliptical in both vertical and horizontal cross-sections with maximum width at the center (Valko and Economides 1995)	Rectangular in the vertical crosssection and elliptical in the horizontal cross-section with constant width (Valko and Economides 1995)
Duration	Long (Gidley and Engineers 1989, Valko and Economides 1995)	Short, small treatments (Gidley and Engineers 1989, Valko and Economides 1995)
Fracture tip effect*	Not considered, focus is on the pressure gradient due to fluid flow in the fracture. Fracture toughness is neglected, as the net pressure for propagation is significantly higher than the fracture toughness pressure (Economides and Nolte 2000)	Is important (Economides and Nolte 2000)
Fracture geometry parameter (A_f)	Half of the half-height ($h_f / 4$)	Half-length (L_f)
Average fracture width (w¯f)	w¯f=(π/5)wf max (Valko and Economides 1995, Rahman and Rahman 2010)	w¯f=(π/4)wf max (Valko and Economides 1995, Rahman and Rahman 2010)

*
The tip effect (fracture toughness) term is negligible compared to $\sigma_{h\,\min}$ (Hwang and Sharma 2013).

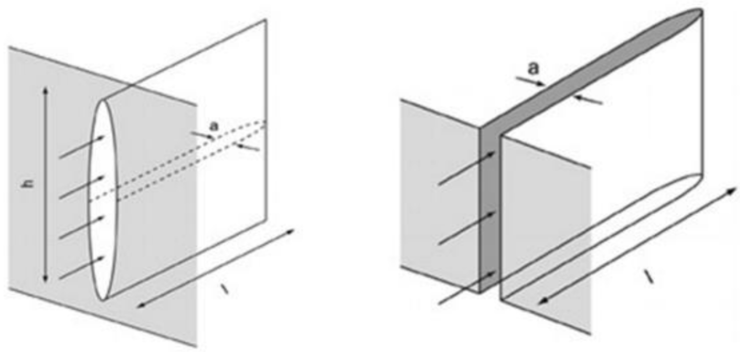

Figure 4—The left plot is the PKN model, and the right plot is the KGD model (Wu et al. 2022).

We assume the fracture height is contained and equal to the reservoir thickness. In polymer flooding field application, the reservoir thickness may range from 10's-100's ft (Sheng 2011, Delamaide et al. 2014, Zechner et al. 2015, Melo et al. 2017, Hwang et al. 2019, Pan et al. 2020, Liu et al. 2020, Sagyndikov et al. 2022). Also, the fracture length depends on reservoir properties, polymer rheology, and operational designs (e.g., reservoir permeability, injected polymer concentration and volume, injection rate, and well-spacing) (Valko and Economides 1995, Economides and Nolte 2000). Therefore, we will consider both KGD and PKN models, keeping in mind that PKN is more appropriate when $2L_f > h_f$ (Valko and Economides 1995, Quosay et al. 2020). Therefore, the KGD fracture model derived by Li et al. (2016) will be utilized in this study, where the KGD fracture equations are presented in **Appendix B**. Following the same derivation approach by Li et al. (2016), the PKN model is also derived in **Appendix C**. The maximum fracture pressure, length, and width are calculated at the wellbore where $x_f = 0$ as follows:

$$p_{net(\max)} = p_{net(\max)-PKN} = \left\{\left(\frac{E'}{2h_f}\right)^{2n+1}\left[\frac{2q_i\left(\frac{2n+1}{n}\right)}{\pi \mathrm{h_f}}\right]^n \left(4C_{Turb}L_f K\right)\right\}^{\frac{1}{2n+2}}, \tag{29}$$

where E'=E1−v2 and C_{Turb} is correction coefficient for turbulance effect (dimeentionless). Note that this net pressure is the pressure drop from the wellbore to the fracture tip. The pressure is calculated assuming a uniform average leakoff; however, the leak-off is non-uniform in reality. Nevertheless, considering the assumption of the homogeneous reservoir, fluid, and geomechanics properties and for model simplicity, we assumed a uniform average leak-off solution. Also, it is believed to have a minor error compared to a computationally expensive non-uniform leak-off solution (Suri et al. 2011, Li et al. 2016).

Meanwhile, the maximum fracture width at the wellbore for PKN model is

$$w_{f\max-PKN} = \left(\frac{2h_f}{E'}\right)\left\{\left(\frac{E'}{2h_f}\right)^{2n+1}\left[\frac{2q_i\left(\frac{2n+1}{n}\right)}{\pi \mathrm{h_f}}\right]^n \left(4C_{Turb}L_f K\right)\right\}^{\frac{1}{2n+2}}, \tag{20}$$

where the average fracture width w¯f=(π/5)wfmax−PKN (Rahman and Rahman 2010, Valko and Economides 1995). Eqs. (19) and (20) can be substituted with the relevant functions for the KGD model as presented in Appendix B.

Coupling UVIM with Fracture Model.

Li et al. (2016) presented a workflow to predict fracture initiation and geometry using viscoelastic polymers that follow the UVM model. Their work was based on the KGD fracture model implemented in chemical flooding reservoir simulator (UTCHEM) (Delshad et al. 1996). UTCHEM was used to update the reservoir properties such as pressure, stresses, permeability, and the injector BHP as the fracture propagates. In our semi-analytical model, we will adopt a similar approach and assumptions. However, we will assume a constant pressure condition at the reservoir boundary, and BHP is updated in UVIM using an equivalent wellbore radius proposed by Prats (1961). Both KGD with PKN models will be considered.

Our simplified fracture model assumptions are.

- The reservoir is homogeneous, single-layer, and single-phase flow (i.e., oil is at residual saturation)
- Radial or "pseudo-radial" flow in a vertical well
- The fracture is vertical with two wings and has a constant height that equates to the reservoir thickness
- Uniform average leak-off from the fracture faces
- The boundary pressure remains constant (P_e), with constant stresses
- Isothermal condition
- Polymer rheology follows a power-law behavior in the fracture
- Constant polymer concentration along the fracture
- Skin factor due to water quality, polymer plugging, and well completion is neglected

Fracture prediction procedure. Prior to fracture initiates, the equivalent wellbore radius (r_{we}) in Eq. (4) is the same as the original wellbore radius (r_w). The prediction of fracture initiation starts once the wellbore bottomhole pressure (BHP) from Eqs.(3) - (5) exceeds the fracture initiation pressure (p_{fi}) from Eq.(10) or (12). The simplified workflow for the PKN model (Fig. 5) is as follows:

1. Calculate the fracture pressure at the wellbore (p_f) from Eqs. (16) and (19)
2. Calculate fracture permeability (k_f) in Eq.(8) using the average maximum fracture width to obtain the average fracture width from Eq.(20)
3. Calculate the relative fluid capacity (a) and equivalent wellbore radius (r_{we}) in Eqs.(9) and (6)
4. Recalculate the *BHP* with UVIM Eq. (4) using the new r_{we}
5. Check the fracture propagation criteria in Eq.(18), and iteratively increase L_f and repeat steps 1-5 until an acceptable tolerance criterion (0 psi $\leq \varepsilon \leq$ 5 psi) is met where 0≤BHP−(KICπAf+pf)≤ε
6. Once an acceptable tolerance criterion is satisfied, move to the next time step and calculate *BHP*, then repeat steps 1 through 5

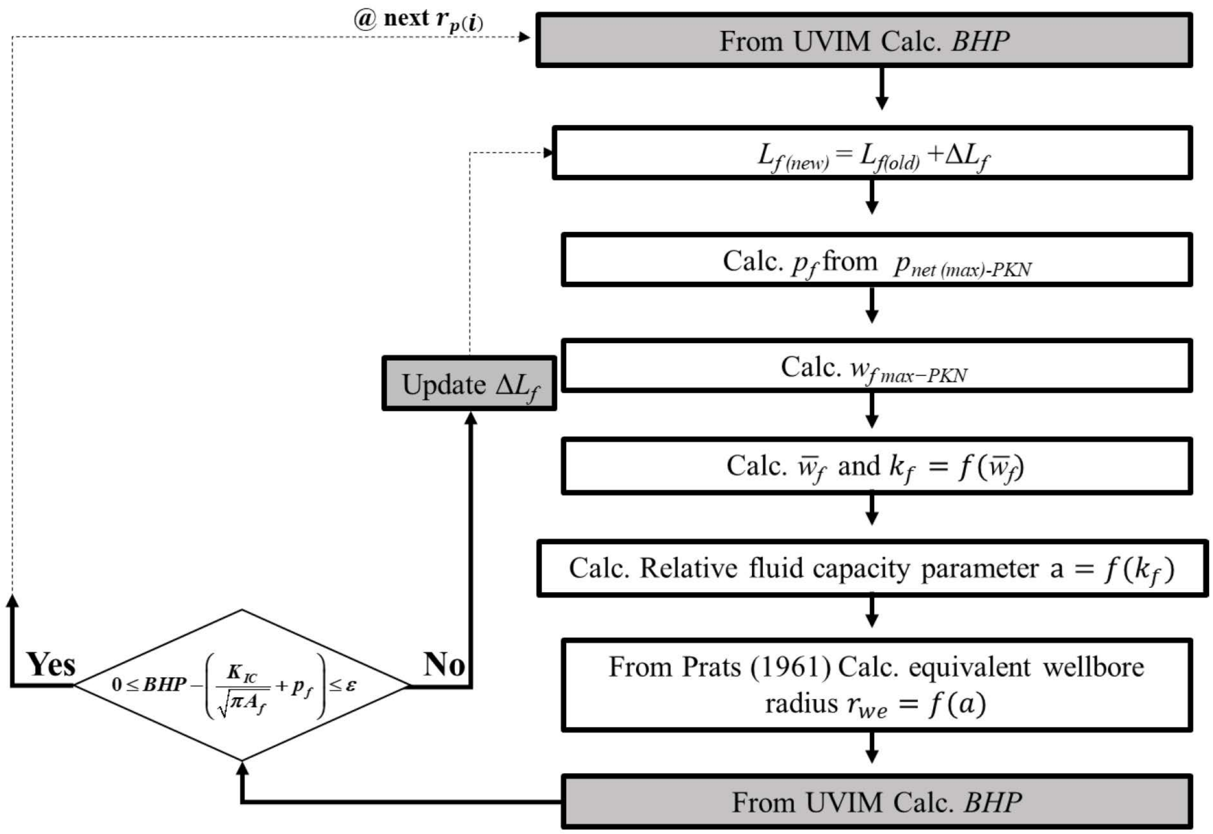

Figure 5—Iterative workflow to predict fracture length and width based on UVIM, PKN fracture model, and equivalent wellbore radius. The same workflow is followed for KGD model but with replacing the maximum fracture net pressure and width ($p_{net(\max)-PKN}$ and $w_{f\,\max-PKN}$) in the third and fourth boxes with KGD values calculated from the equation for $p_{net(\max)-KGD}$ and $w_{f\,\max-KGD}$ in Appendix B.

The workflow for KGD model is the same, but with replacing the maximum fracture net pressure and width (Eqs. (19) and (20)) in steps 1 and 2 with the KGD equations in Appendix B.

Coupling Fracture Model with Elastic Desaturation Curve

Qi et al. (2018) proposed an elastic desaturation curve (EDC) that correlated Deborah number to residual oil-saturation reduction based on 20 corefloods. The correlation assumes polymers have significant elasticity when $N_{De} > 1$ (Hirasaki and Pope 1974, Erincik et al. 2018, Chiyu et al. 2022).

$$\frac{S_{orp}}{S_{orw}} = \begin{cases} 1 & \text{if } N_{De} < 1 \\ 1 - 0.133 \log N_{De} & \text{if } N_{De} \ge 1 \end{cases}, \tag{21}$$

where S_{orp} is remaining oil saturation after viscoelastic polymer injection. The Deborah number is calculated as:

$$N_{De} = \gamma_{eff}\tau. \tag{22}$$

The insitu relaxation time (τ) is obtained by fitting Eq. (1). Meanwhile, the effective shear rate (γ_{eff}) is calculated from Eq.(24) by replacing the Darcy velocity with the average flux through the fracture walls as follows:

$$flux = \frac{q_i}{4h_f L_f}. \tag{23}$$

Results and Discussion

Analytical Model Verification with Numerical Simulation

In this section, the proposed analytical injectivity and fracture model is verified with two fracture models from the literature: the Complex Fracturing Research Code simulator (CFRAC) (Ma and McClure 2017), and the University of Texas Well Injectivity Decline simulator (UTWID) (Gadde and Sharma 2001). Then, a verification with a constructed CMG-GEM model is discussed.

Verification with CFRAC. Ma and McClure (2017) developed a 2-D discrete-fracture-network single-well simulator, which couples fluid flow with stress variation during fracturing (Complex Fracturing Research Code or CFRC). The main objective of the model is to predict the change in injectivity due to polymer shear thinning and thickening insitu rheology. The model does not present a quantitative measurement of fracture geometry but rather fracture initiation only. It is a single-phase model that assumes, prior to polymer injection, water is injected until reaching a steady state pressure gradient with a constant boundary pressure. Unsteady-state mass-balance equation is applied in the matrix with Darcy's law. The fluid flow and the mass balance between the matrix and fracture are solved using the finite volume method. The polymer rheology in the matrix follows the UVM, while the polymer rheology in fractures follows the Carreau model (Carreau 1972).

Ma and McClure (2017) simulated polymer injectivity with a radial flow in a 1312 ft ^{z}1312 ft 2-D Cartesian model. They presented two similar cases but with a variation in minimum horizontal stresses, ranging from 2900 psi 3770 psi. The main objective is to observe the change in injectivity as a function of polymer rheology at the early injection period once the fracture is initiated. Our objective is to verify the proposed analytical model results using the PKN and KGD fracture models. The model input parameters are presented in Table D-1.

It is worth noting that Ma and McClure (2017) selected a grid size of 6.5ft × 6.5ft, which is considered a coarse grid for polymer flooding (Aitkulov et al. 2021). Li and Delshad (2014) and Aitkulov et al. (2021) discussed that in polymer flooding, a coarser grid near the wellbore smears out fluid velocity. As a result, for a viscoelastic polymer, the polymer viscosity is in the shear thinning region (i.e., lower velocity or shear rate) than shear thickening, leading to a lower viscosity and higher polymer injectivity than our analytical model results (Fig. 6 (a) and Fig. 7 (a)). On the contrary, for a shear thinning rheology polymer, a lower velocity results in a higher viscosity than the analytical solution, as seen in Fig. 7 (b). Applying a minimum horizontal stress of 3770 psi using the UVIM-PKN model resulted in a small fracture of about 3 ft in the shear thinning and thickening polymer rheology. At the same time, no fracture was observed with the UVIM-KGD model (Fig. 6 (a)). For the shear thinning polymer rheology in Fig. 6 (b), both PKN and KGD fracture models showed no fracture was initiated. Meanwhile, Ma and McClure (2017) predicted fracture was initiated at a later time of about 75 days, which can be explained by the higher viscosity calculated from their coarse grid.

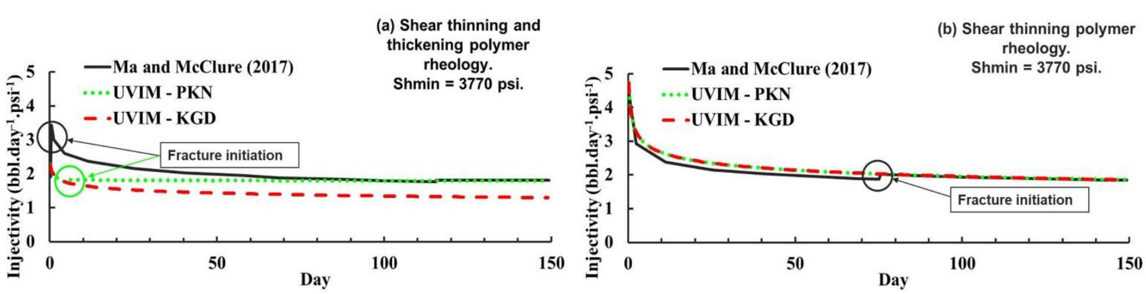

Figure 6—Comparison between well injectivity at minimum horizontal stress of 3770 psi calculated from Ma and McClure (2017) model in the solid-black line, UVIM-PKN model in the green-dotted line, and UVIM-KGD model in the red-dashed line. (a) shear thinning and shear thickening polymer rheology model, while (b) shear thinning polymer rheology only.

Fig. 7(a) and 7(b) indicate that fracture enhanced injectivity by two and three folds without and with shear thickening rheology, respectively. In Fig. 7 (b), we notice a delay in fracture initiation with the UVIM-KGD model compared to UVIM-PKN. The latter can be explained by the fact that the fracture pressure in the PKN model is positively proportional to fracture length. Meanwhile, in the KGD model, it is negatively proportional to fracture length (see Fig. 8 (a) and Eqs. (19) and (30)). As per Eq. (18), the fracture is initiated when the initial fracture pressure intersects with the BHP. As a result, a 10-day delay in initiating the fracture can be observed when using the KGD fracture model, as seen in Fig. 8 (b), as the bottomhole pressure (BHP) increases to meet the criteria for fracture initiation. A similar observation was made by Li et al. (2016) when they compared their KGD-based model with a PKN-based model.

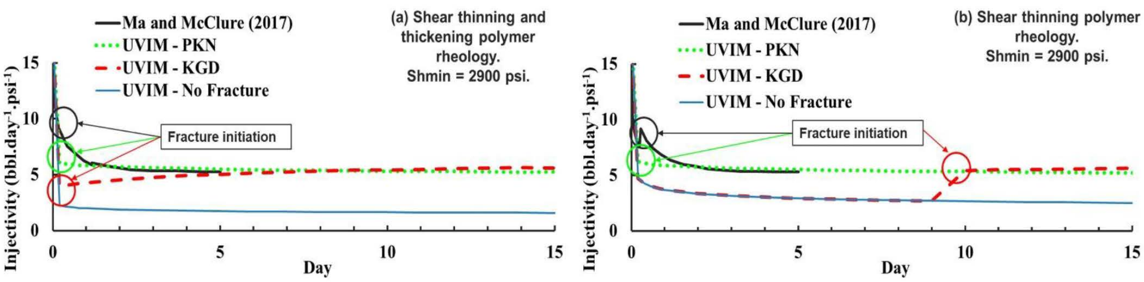

Figure 7—Comparison between well injectivity at minimum horizontal stress of 2900 psi calculated from Ma and McClure (2017) model in the solid-black line, UVIM-PKN model in the green-dotted line, UVIM-KGD model in the red-dashed line, and UVIM without fracture permitted in thin blue line. (a) shear thinning and shear thickening polymer rheology model, while (b) shear thinning polymer rheology only. Note: Ma and McClure (2017) data are only provided for five days.

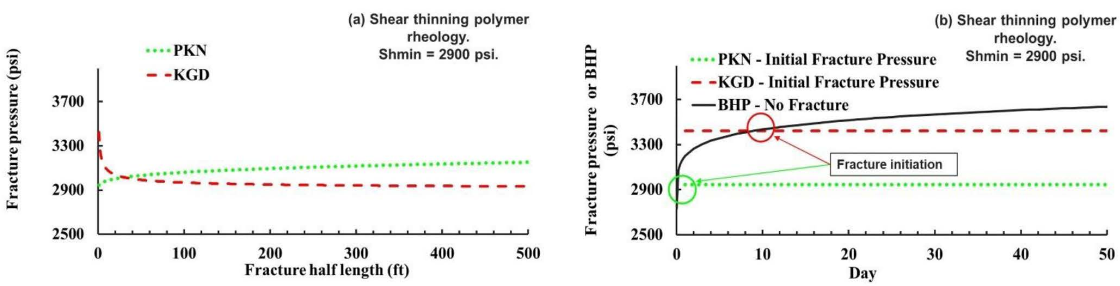

Figure 8—Differences between PKN and KGD fracture model at minimum horizontal stress of 2900 psi with shear thinning rheology only. (a) fracture pressure as a function of fracture half-length calculated using PKN (green dotted line) model and KGD (red dashed line). (b) The bottomhole pressure (BHP) was calculated without permitting fracturing in the black line. The circles illustrate the fracture initiation criteria when the fracture pressure from PKN (green dotted line) and KGD (red dashed line) intersect with the BHP.

Verification with UTWID. Gadde and Sharma (2001) constructed a single-well numerical simulator to predict fracture geometry during water flooding (UTWID). The model accounts for practical plugging, changes in thermal stresses, and the impact of changes in pore pressure (Suri and Sharma 2009, Suri et al. 2011). UTWID is based on PKN fracture model (Nordgren 1972). Polymer viscosity is calculated using a simple power-law model for shear thinning and shear thickening behavior. The model accounts for stress variations as the reservoir pressure changes during fracturing (Hwang et al. 2019).

Li et al. (2016) presented three synthetic cases to predict fracture length for a homogeneous-isotropic reservoir model using UTWID with variable drainage radii of 500, 1000, and 1500 ft. A 0.5 PV polymer slug is injected (85 days) with a concentration of 1500 ppm at 356 bbls/day. Reservoir and fluid properties are presented in Table D-2. From Fig. 9, we observe that our fracture model in solid lines provides a qualitatively good match with UTWID prediction. The quantitative mismatch can be attributed to pressure drop calculation in the water-flooded zone. Our model assumes that the whole reservoir is flooded to residual oil saturation prior to polymer injection (referred to in Fig. 1). As such, from Eq. (5) the pressure drop in the water flooded zone is calculated at k rw0=0.3, resulting ΔPw = 290 psi. Meanwhile, in UTWID, the oil saturation prior to water injection is at Soi where krw < k rw0. For example, at initial polymer injection, let us assume $k_{rw} = 0.05$ then $\Delta P_w = 1700$ psi. The impact of ΔP_w is more pronounced for a larger drainage radius of 1500 ft. Another factor for the mismatch, especially at a smaller drainage radius (i.e., 500 ft), is the impact of the constant reservoir pressure assumption in our model. On the contrary, UTWID assumes reservoir pressure increases when the polymer is injected. Therefore, a higher BHP will build up to overcome the poroelastic stress impact leading to a shorter fracture (Hwang et al. 2019). A similar observation was found by Li et al. (2016), when using a constant boundary condition.

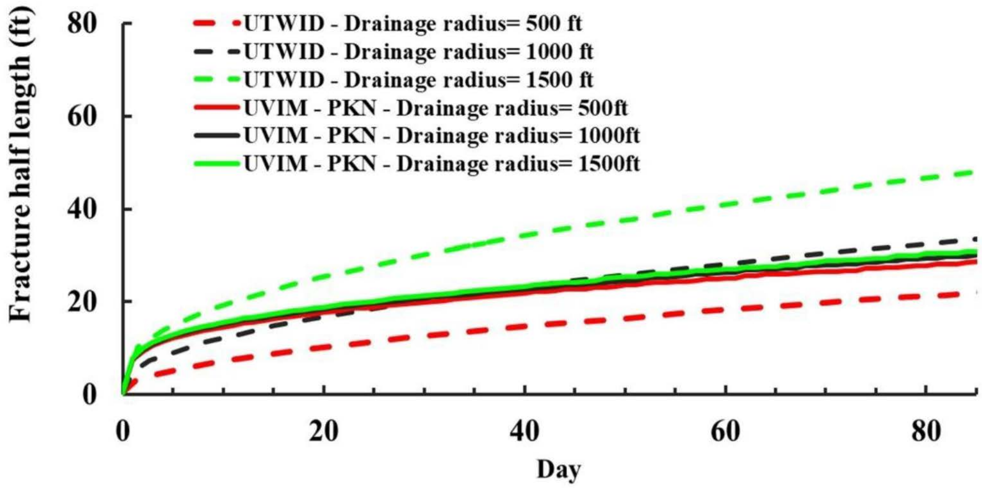

Figure 9—Comparison between fracture half-length predicted by our UVIM-PKN model in solid lines with UTWID model in dashed lines for drainage radii 500, 1000, and 1500 ft. 1500 ppm HPAM polymer is injected for 85 days at 356 bbls/day.

Verification with CMG-GEM. This step aims to comprehend better the discrepancies between numerical models and our analytical model. Also, to corroborate the earlier identified observations in mismatching the literature fracture models: CFRAC and UTWID. Our analytical injectivity model UVIM has been matched with a 2-D radial CMG-GEM model that is homogeneous with a drainage radius of 267ft at constant boundary pressure of 2000 psi (Table D-3). We used the same radial gridding strategy detailed in Tables 3 and 4 in our previous work (Abdullah et al. 2023). Assuming oil is at residual saturation, the polymer solution was injected for 50 days at 1000 bbls/day. In CMG-GEM, the viscoelastic polymer rheology is in tabulated form (Table D-4). Also, the apparent shear rate equation is slightly different from Eq. (24) in

Appendix A; therefore, the correction factor in CMG (SHEAR FAC) had to be adjusted to 4.2 (CMG 2022).

Cartesian coordinate grid is required to predict fracture propagation in CMG-GEM to overcome a limitation in the current CMG-GEM version to model polymer flooding in the radial coordinate when coupled with geomechanics module. Therefore, examining the impact of grid size on injectivity was essential for both shear-thinning and viscoelastic polymers in the absence of fractures. As shown in Fig. 10 (a) for shear-thinning polymer rheology, considering the radial coordinate as a reference, the bottomhole pressure increase when the grid size increases. This results from the fact that when grid size increases, the shear rate decreases, and polymer shear thinning viscosity increases. On the contrary, for a viscoelastic polymer Fig. 10 (b), as the shear rate decreases, the polymer shearthickening viscosity decreases, resulting in lower bottomhole pressure. Furthermore, this study found that the smallest grid size of 3ft × 3ft is the best grid size compared to the radial model (Table D-5). This finding agrees with our earlier discussion on the impact of coarse grid sizes on over/under-predicting injectivity in Ma and McClure (2017) study.

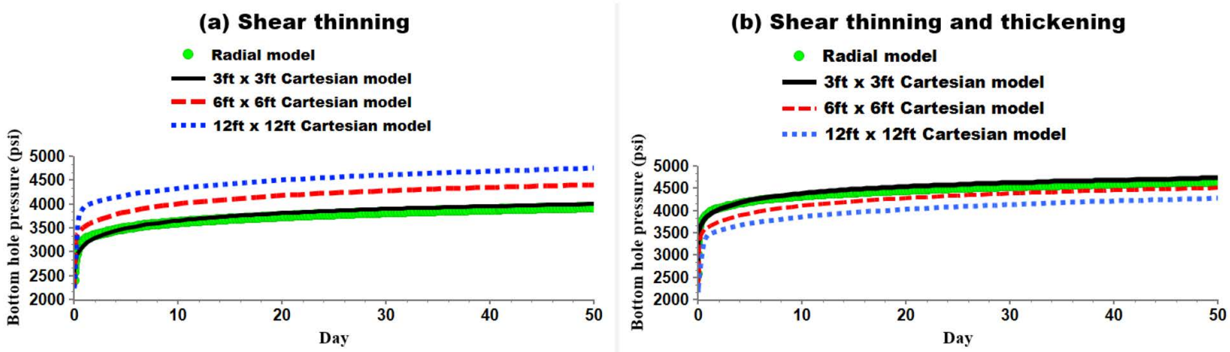

Figure 10—The impact of Cartesian grid size (3ft × 3ft in solid black line, 6ft × 6ft in dashed red line, and 12ft × 12ft in blue dotted line) on bottomhole pressure in comparison to the radial grid in green circles. (a) bottomhole pressure with shearthinning rheology, and (b) bottomhole pressure with shear-thinning and shear-thickening rheology.

Water flooding prior to polymer injection is a common practice in field development to minimize reservoir geological uncertainties before polymer flooding (Rashid et al. 2018, Wu et al. 2019, Cocco et al. 2020, Al-Dhuwaihi et al. 2022). Therefore, our analytical model assumes the polymer is injected at waterflooding residual oil saturation. However, to investigate the impact of two-phase flow on polymer injectivity and fracture extension, discussed in the verification with the UTWID model section, we compared the injection of the polymer at initial oil saturation (secondary flood) versus at residual oil saturation (tertiary flood) in CMG-GEM. We utilized a 3ft × 3ft Cartesian coupled fluid-flow-geomechanics model, with input parameters detailed in Table D-5. It is worth noting that the CMG-GEM fracture initiation is based on linear Mohr-Coulomb failure criteria (Paul 1968). Also, fracture propagation is permitted when the effective stress reduces below a user-defined tensile fracture criterion (Tran et al. 2008, Tran et al. 2013). We applied the same horizontal stresses in UVIM-PKN and CMG-GEM models, and tuned the tensile criterion (TENFRAC) to match our analytical model fracture initiation and extension for further sensitivity studies (Table D-5). Fig. 11 shows the coupled fluid and geomechanics grids for the base case of 3ft × 3ft at residual oil saturation. The CMG-GEM geomechanics grids (Fig. 11 (b)) predicted a fracture half-length of ~60ft compared to the analytical UVIM-PKN of 56 ft at the end of injection at day 50.

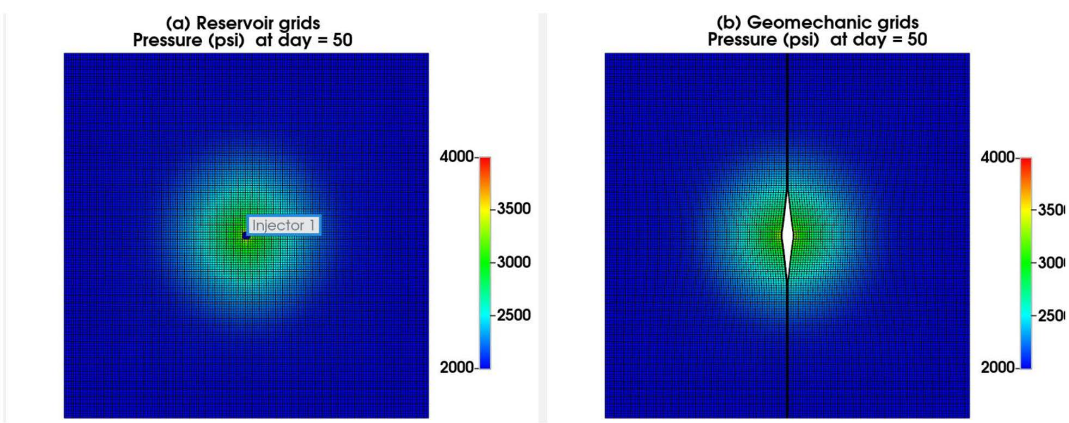

Figure 11—Pressure distribution (psi) at day 50 in the coupled model of 3ft × 3ft. (a) reservoir grids with a central well, and (b) geomechanics grid showing a magnified view of fracture geometry with a fracture half-length of 60ft.

As anticipated, Fig. 12 and Fig. 13 demonstrate that two-phase flow resulted in higher bottomhole pressure (BHP) and more extensive fracture than single-phase flow, per our previous discussions. In the two-phase case, given the higher oil saturation, the total mobility of the phases in the porous medium is greater, requiring a higher BHP for the same target injection rate. Notably, in Fig. 12 (b), the injector bottomhole pressure for CMG-GEM models exceeds that of our UVIM-PKN model after fracture initiation, due to the previously discussed differences in fracture propagation criteria. Fig. 13 highlights the excellent agreement between the UVIM-PKN model and the CMG-GEM solution for the fracture half-length in the case with residual oil saturation, allowing us to apply the UVIM-PKN model to field data in the next section.

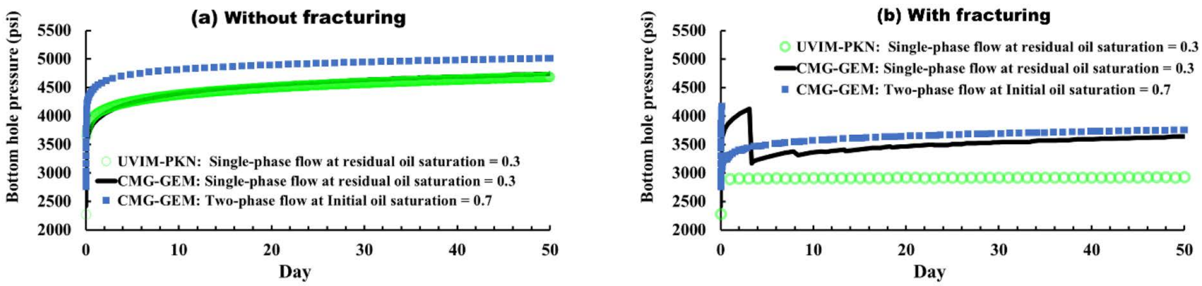

Figure 12—Comparison between bottomhole pressure for a single-phase flow at residual oil saturation (analytical UVIM-PKN model in green circles and CMG-GEM in solid black line, and the two-phase flow CMG-GEM model in blue squares.(a) bottomhole pressure without permitting fracturing, and (b) permitting fracturing.

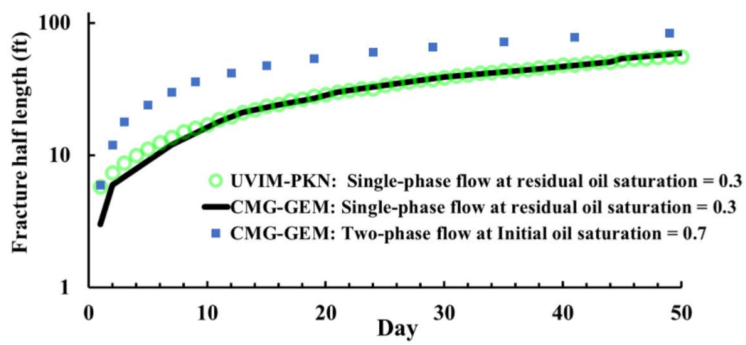

Figure 13—A semi-log plot comparing fracture half-length for a single-phase flow at residual oil saturation (analytical UVIM-PKN model in green circles and CMG-GEM in solid black line), with the two-phase flow (CMG-GEM model in blue squares).

Field Case Study: Matzen Field

The HPAM polymer (FP3630) was injected into a vertical well in the Matzen field for about 53 days, after a long period of waterflooding. The formation parting pressure (FPP) recorded from a fall-off test was about 2650 psi, prior to polymer injection. The polymer is assumed to be mechanically degraded based on lab tests that simulated the near wellbore velocities. Mechanical degradation of polymer showed a severe reduction in the maximum extensional viscosity from ~160 cp to ~30 cp (Gumpenberger et al. 2012, Zechner et al. 2013, Clemens et al. 2013, Zechner et al. 2015). Nevertheless, to history-match the observed injectivity enhancement during field polymer injection, an induced fracture is expected to initiate in the 16-ft thick reservoir (Hwang et al. 2019). In this section, we will predict the fracture length for the Matzen's vertical well with our fracture model and conduct a sensitivity study to highlight how reservoir permeability impacts fracture extension.

Fracture Length Prediction. Hwang et al. (2019) predicted a fracture extension of about 220 ft from the vertical injection well in Matzen oilfield using the UTWID model with a simplified power-law viscoelastic polymer rheology. We used our UVIM-PKN model to predict and verify fracture extension with the UTWID model, which is also based on the PKN fracture model. A constant polymer concentration of 1000 ppm is injected at a constant rate of 2400 bbls/day for 53 days into a 16-ft thick formation. The reservoir and polymer properties are summarized in Table D-6, and more details can be found in (Clemens et al. 2013, Zechner et al. 2015, Hwang et al. 2019).

It is important to note that the computation of the effective shear rate by Hwang et al. (2019) assumes no shear rate correction factor (C = 1) and divides the effective shear rate Eq.(24) by 4. As a result, lower viscoelastic viscosity near the wellbore is expected with a lower effective shear rate. Therefore, we adjusted Eq.(24) in

Appendix A accordingly. The calculation of the effective shear rate is a controversial topic in the literature. The model is based on the capillary bundle approach, which has been modified in various ways by different researchers according to laboratory observations. More details are provided by Skauge et al. (2018).

From Fig. 14 (a), the predicted fracture length by the UVIM-PKN model qualitatively agrees with UTWID model (Hwang et al. (2019)). It is no surprise to observe a quantitative disparity between the two models that can be ascribed to several causes. Our model assumed a constant average injection rate through the polymer injection period. Meanwhile, the UTWID model considered the actual field injection rate (shown in Fig. 14 (b)), which causes the oscillation in fracture extension. The mismatch in the first ten days can be due to higher actual injection rate, skin factor considered in UTWID, and prior fracture existence during waterflood reported by Hwang et al. (2019), which can change stresses in UTWID. Also, UTWID accounts for poroelastic stress changes during polymer injection. Thus, as the polymer is injected, reservoir pressure increases and minimum stress increases subsequently. Therefore, our model may predict longer fractures with lower minimum stress than UTWID. A good history matching of the actual field results is achieved by the UVIM-PKN model while assuming a constant injection rate of 2400 bbls/day (Fig. 14 (b)). The early-time BHP mismatch can be due to the gradual and interpreted polymer injection rate in the field reported by Zechner et al. (2015).

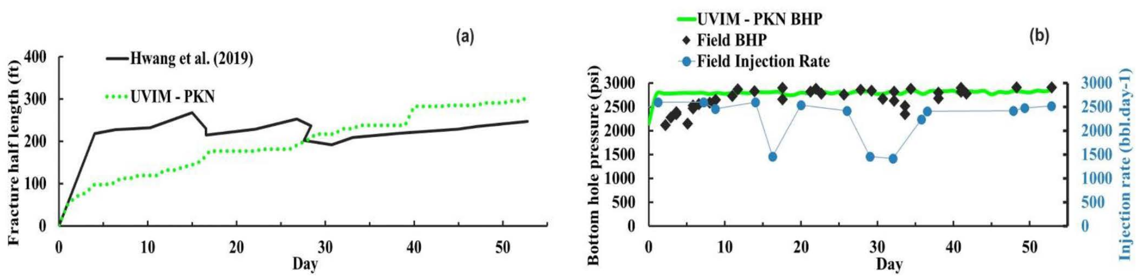

Figure 14—(a) comparison between predicted fracture extension by Hwang et al. (2019), UTWID model in black solid-line, and UVIM - PKN model in green dotted line. (b) History matching of measured bottomhole field pressure in black rhombus and UVIM -PKN model predicted pressure in the green line. The connected blue circles show the recorded field injection rate.

Polymer Elastic Desaturation. Especially under conditions associated with near-wellbore velocities, some lab studies have demonstrated that viscoelastic polymer can enhance microscopic sweep efficiency by reducing waterflood residual oil saturation (Qi et al. 2017, Erincik et al. 2018, Koh et al. 2018, Jin et al. 2020, Mohamed et al. 2023). During a field-scale polymer flood in the Daqing field, injecting polymers with greater viscoelasticity was proposed to reduce residual oil saturation and increase oil recovery (Wang et al. 2008, Guo et al. 2021). Studies associated with other reservoirs and conditions indicate no reduction of capillary-trapped residual oil during polymer flood (e.g., Seright et al. (2018)). At the same time, higher viscoelasticity of polymer entails higher concentration and larger molecular weight, which can be constrained in the field by the well injectivity (Seright et al. 2009, Azad and Trivedi 2019b, Azad and Trivedi 2020, Abdullah et al. 2023). Therefore, when high viscoelastic polymers are injected above the parting pressure, fractures are induced, and the extensional polymer behavior will be surpassed by shear thinning rheology in fractures (Li et al. 2016, Ma and McClure 2017, Hwang et al. 2019). Therefore, we are trying to examine for the Matzen field case if the reduction in residual oil saturation is still expected post-fracture initiation. As discussed earlier, to address this question, we coupled our fracture model with Qi et al. (2018)'s elastic desaturation curve (EDC) that empirically correlates Deborah number to residual oil-saturation reduction. Although the EDC curve is nonuniversal across different polymers, it may be suitable for the FP-3630 polymer utilized under the particular conditions assumed in this study. Furthermore, it is a convenient method to distinguish the oil recovery attributed to polymer elasticity beyond waterflood residual oil saturation.

We can observe from Fig. 15 (a) that as soon as the fracture is initiated, the insitu effective shear rates decrease from over 1000 s^{-1} to about 1 s^{-1}. As a result, the Deborah number in Fig. 15 (b) reduces from 100's to less than around 3. This observation can explain the insignificant additional recovery (< 1%) observed from polymer viscoelasticity using EDC, once the fracture is initiated.

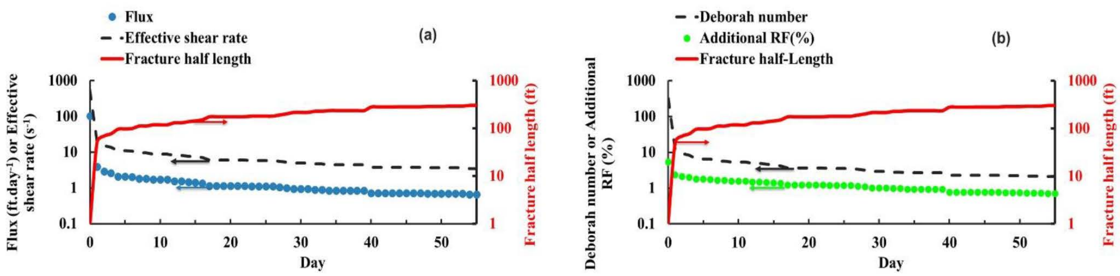

Figure 15—(a) a log-normal plot of fracture half-length extension (red line) and its impact on flux in the fracture (blue dots) and effective shear rate (dashed line). (b) a plot of fracture half length (red line) extension and its impact on the Deborah number (dashed line) and additional recovery factor (RF) (green dots) calculated from the EDC. All calculations are from the UVIM- PKN model.

Impact of Formation Permeability on Fracture Length. As previously mentioned, the increase of aqueous phase viscosity near the wellbore by polymer elongational viscosity reduces well injectivity until the fracture is initiated, leading to injectivity enhancement. Still, fractures need to be contained within one-third of the injector-producer distance to maintain good sweep efficiency (Dyes et al. 1958, Seright 2017). Therefore, formation permeability is one of the key parameters in reservoir screening for polymer flooding (Taber et al. 1997, Lake et al. 2014). Most of the reported polymer flooding field cases have a formation permeability of over 100 mD (Sagyndikov et al. 2022). Using our UVIM-PKN model, we tested the impact of formation permeability on fracture initiation and propagation for the Matzen field vertical well. The FP-3630 polymer at a constant concentration of 1000 ppm was injected at 2400 bbls/day into a 550 mD and 16.5 ft formation. The reservoir permeability was varied by a factor of 0.1 to 10 of the original permeability.

Interestingly, the case with 55 md resulted in an early fracture of about 460 ft half length during the waterflooding prior to the polymer flooding (Fig. 16). This observation is not surprising considering the high injection rate into a thin and low permeability formation. By reducing the permeability from 550 mD to 275 mD, the fracture half length extended to 723 ft, almost triple the original case with 296 ft fracture half length. When doubling the permeability from 550 mD to 1100mD, the fracture half length is reduced to 55 ft, five times less than the original case. No fracture was initiated when increasing the permeability to 1100 mD. From the previous two cases, we can highlight that for field implementation, to improve microscopic efficiency from polymer viscoelasticity, induced fractures need to be avoided. Therefore, selecting a high permeability reservoir with an optimum injection rate design may result in high polymer viscoelasticity.

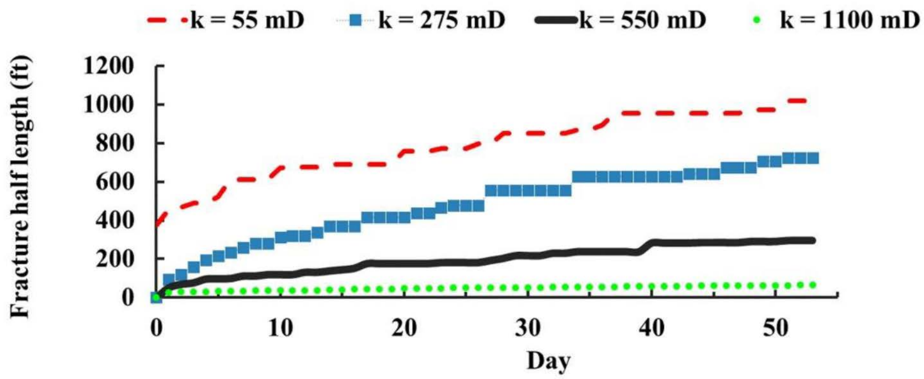

Figure 16—Impact of formation permeability variations on fracture initiation and extension using UVIM-PKN model.

Uncertainty in Relaxation Time Estimation: Debating Methods, Assumptions, and Insitu Rheology Dependencies

As shown in this study, relaxation time is crucial for predicting the onset of polymer shear thickening and elastic desaturation. Unfortunately, there remains a lack of consensus regarding the alignment of insitu relaxation time measurements with rheological measurements, as reported by Azad and Trivedi (2019b) and Azad and Trivedi (2020). The crosspoint (oscillatory) method has been proposed by various researchers (Delshad et al. 2008, Ehrenfried 2013, Koh 2015). Conversely, the crosspoint method has been critiqued for its assumption of a linear viscoelastic model. This has led to alternative suggestions, such as employing a capillary break-up rheometer with the Maxwell model (Azad and Trivedi 2019a), or utilizing a cone-and-plate rheometer upturn point (Howe et al. 2015, Azad 2022).

Moreover, while deriving relaxation time directly from core flood experiments might be more rigorous, its value remains an estimation and a continuous debate in the literature. Chauveteau (1981) and Heemskerk et al. (1984) agree that relaxation time signifies the inverse of the shear rate at which rheology departs from shear-thinning power-law behavior. Typically, this critical onset shear rate corresponds to a critical Deborah number of ~ one. Lohne et al. (2017) provide a useful definition of a critical Deborah number of one as: "It does not describe the actual onset of elongation at pore entrance, but rather the situation where polymer molecules have insufficient relaxation time to recover from its distortion in the previous pore throat before entering the next". However, as per Eq. (22), the magnitude of relaxation time depends on the selected equation for the equivalent shear rate, which is another debated issue (Skauge et al. 2018). The UVM (Delshad et al. 2008) suggests that the relaxation time can be derived from the crosspoint experiment or estimated from fitting the coreflood polymer viscoelastic flow curve. Consequently, the fitted UVM relaxation time does not correspond to the minimum viscosity point (actually minimum resistance factor) but approximates the relaxation time at the initiation of viscoelasticity. Seright et al. (2023) propose that there may be a considerable value in developing methods to relate rheological measurements to the minimum resistance factor- versus-velocity curve—since that is the easiest and most reliable point to relate to during corefloods. Seright et al. (2023) also point out critical inconsistencies associated with the presence of residual oil during previous literature reports—and their potential importance when predicting the degree of fracture extension and reduction of capillarytrapped residual oil. These inconsistencies concern (1) whether or not the presence of residual oil shifts the onset of shear thickening in a manner consistent with expectations from the reduction of relative permeability to water, (2) the magnitude of resistance factors above the onset of shear thickening, and (3) the magnitude of resistance factors below the onset of shear thickening.

Another critical aspect is the need for a comprehensive study that addresses a central debated question: how does "insitu" relaxation time vary with reservoir and operational conditions such as polymer concentration, brine salinity, temperature, and oil saturation? To the best of our knowledge, existing comprehensive studies in the literature primarily rely on rheological measurements or microfluidic model conditions (Briscoe et al. 1999, Jiang et al. 2003, Hincapie et al. 2017, Rock et al. 2020, Aliabadian et al. 2022), which may not accurately represent the porous media conditions. Furthermore, other studies approached contradictory findings. For example, while some suggested that relaxation time is dependent on polymer concentration (Qi 2018, Kim et al. 2010, Jin et al. 2020), others indicate that it is not (Howe et al. 2015). Therefore, in our complementary study (Seright et al. 2023), we carry out a series of core flood experiments utilizing FP-3630 under various conditions to shed light on unresolved issues concerning relaxation time, especially as a function of residual oil saturation, salinity, and temperature.

Summary and Conclusions

In this paper, a physics-based analytical model was developed to predict polymer injectivity and fracture length during polymer flooding. The model is based on the unified viscoelastic model coupled with two 2-D fracture models (PKN and KGD) and the elastic desaturation curve to model the reduction in waterflood residual oil saturation. Below are the main conclusions of this work:

1. The injectivity-fracture model proposed in this paper (UVIM-PKN and UVIM-KGD) showed reasonable qualitative agreement with the numerical models CFRAC, UTWID, and CMG-GEM reservoir simulator. In the latter case, it is also possible to compare the fracture half-length in the same oil saturation condition with excellent results
2. Fracture initiation due to extensional viscosity improves vertical well injectivity. Still, fracture length prediction is a crucial aspect of polymer flooding that has been addressed in this study. UVIM-PKN model demonstrated good fracture length prediction for a vertical well in the Matzen field.
3. The improvement in microscopic efficiency due to polymer viscoelasticity may be diminished by fracture initiation.
4. Sensitivity analysis on the impact of reservoir permeability on fracture length in the Matzen field demonstrated that fracture length is highly sensitive to formation permeability. In fact, permeability reduction from 1100 mD to 55 mD leads to fracture half length increase from 55 ft to 723 ft.
5. The developed tool can assist field operators in reducing uncertainty and risk in polymer injectivity and quantifying fracture extension into the reservoir.

Acknowledgment

The first author would like to recognize Kuwait University's financial support, which enabled him to pursue his Ph.D. at the University of Texas at Austin. The authors would like to thank Dr. Mukul Sharma for his unwavering support in the derivation of UVIM fracturing model.

Nomenclature

1-D	one dimensional
2-D	two dimensional
CFRC	Complex Fracturing Research Code
EOR	enhanced oil recovery
HPAM	partially hydrolyzed polyacrylamide or acrylamide-acrylate copolymer
KGD	Kristianovich-Geertsma-de Klerk
PKN	Perkins-Kern-Nordgren
UTWID	University of Texas Well Injectivity Decline simulator
UVIM	unified viscoelastic injectivity model
UVM	unified viscoelastic model
A_f	fracture geometry parameter, ft

a relative capacity parameter, unitless
BHP bottomhole pressure, psi, [Pa]
C insitu shear rate correction factor
C_{11} water volume fraction in the water phase, volume.volume-1
C_{51} total anions, mEq.mL-1 or meq.mL-1
C_{61} total divalent cations, mEq.mL-1 or meq.mL-1
C_p polymer concentration, wt%
C_{Turb} correction coefficient for turbulence effect, unitless
C_{SEP} effective salinity, meq.mL-1
E Young's modulus, psi [Pa]
F_{CD} fracture conductivity, unitless
h reservoir thickness, ft [m]
h_f fracture height, ft
K power-law coefficient, psi.sec^{n-1}
K_{IC} fracture toughness, psi.inch$^{0.5}$
k permeability, mD [m^2]
k_f fracture permeability, darcys [μm^2]
k_p polymer permeability, mD [m^2]
k_{rw} water relative permeability, unitless
k_w water permeability, mD, [m^2]
N_{De} Deborah number, dimensionless
n shear thinning index, unitless
n_2 exponent associated with the shear-thickening behavior, unitless
n_p power-law exponent, unitless
P_e boundary pressure, psi
$p_{net(\max)}$ maximum fracture net pressure, psi [Pa]
p_f fracture pressure, psi [Pa]
p_{fi} fracture initiation or breakdown pressure, psi [Pa]
p_{res} pore or reservoir pressure, psi [Pa]
p_{tip} pressure at the fracture tip, psi [Pa]
q injection rate, [m^3/sec]
R_k permeability reduction factor, unitless
r_e boundary radius, ft [m]
r_p polymer slug radius, ft [m]
r_{wD} dimensionless effective wellbore radius, unitless
r_{we} equivalent wellbore radius, ft [m]
S_{orp} remaining oil saturation after viscoelastic polymer injection, untiless
S_{orw} residual oil saturation, untiless
S_w water saturation, untiless
s_p polymer salinity slope, unitless
T temperature, °F [°K]
T_0 tensile strength, psi [Pa]
U_r Darcy velocity, ft/day [m/sec]
x_f distance from the wellbore to an arbitrary point along the fracture, ft [m]
w¯f average fracture width, ft [m]
$w_{f\max}$ maximum fracture width, ft [m]

$w_{f\,\max\text{—}KGD}$ maximum fracture width from KGD model, ft [m]
$w_{f\,\max\text{—}PKN}$ maximum fracture width from PKN model, ft [m]
τ approximates insitu viscoelastic relaxation time, sec
μ_{max} maximum polymer viscosity in shear-thickening, cp [mPa s]
λ_2 shear-thickening parameter = 0.01, unitless
λ shear-thinning parameter, sec^{-1}
v Poisson's ratio, unitless
ΔP_T total pressure drop, psi [Pa]
ΔP_p polymer pressure drop, psi [Pa]
Δp_{res} change in reservoir pressure, psi [Pa]
ΔP_w water pressure drop, psi [Pa]
μ_{app} apparent polymer viscosity, cp [mPa s]
μ_∞ polymer viscosity at high shear rate, cp [mPa s]
μ_p polymer viscosity, cp [mPa s]
μ_w water viscosity, cp [mPa s]
μp0 zero-shear rate polymer viscosity, cp [mPa s]
$\sigma_{h\,\max}$ are maximum horizontal stress, psi [Pa]
$\sigma_{h\,\min}$ minimum horizontal stress, psi [Pa]
α Biot's poroelastic constant, unitless
$\dot{\gamma}$eff effective shear rate in the reservoir, sec^{-1}
β_p fitting parameter describing divalent to anions effectiveness, dimensionless
Mw molecular weight, Mg/mol [M Daltons]
η poroelastic constant, unitless
ϕ porosity, unitless
$\dot{\gamma}$ shear rate, sec^{-1}
ε tolerance criterion, psi [Pa]
β unit conversion from ft^2 to mD (9.413×10^{13})

References

Abdullah, M. B., Baqer, S., Delshad, M. et al 2023. Unified Viscoelastic Injectivity Model: Analytical Solutions Predicting Polymer Excess Pressure and Fracture Initiation. *Geoenergy Science and Engineering* **221**: 111259. https://www.sciencedirect.com/science/article/pii/S0920410522011111.

Abramowitz, M., Stegun, I. A., and Romer, R. H. 1988. Handbook of Mathematical Functions with Formulas, Graphs, and Mathematical Tables. *American Journal of Physics* **56** (10): 958–958. https://doi.org/10.1119/1.15378.

Aitkulov, A., Edwards, R., Delamaide, E. et al 2021. An Analytical Tool to Forecast Horizontal Well Injectivity in Viscous Oil Polymer Floods. *Journal of Petroleum Science and Engineering*: 108748. https://www.sciencedirect.com/science/article/pii/S0920410521004083.

Al-Dhuwaihi, A.-A., Tiwari, S., Baroon, B. et al 2022. Mapping Chemical EOR Technologies to Different Reservoir Settings at Harsh Conditions in North Kuwait. Presented at the SPE Improved Oil Recovery Conference. https://doi.org/10.2118/209471-MS.

Al-Murayri, M. T., Kamal, D. S., Al-Sabah, H. M. et al 2019. Low-Salinity Polymer Flooding in a High-Temperature Low-Permeability Carbonate Reservoir in West Kuwait. Presented at the SPE Kuwait Oil & Gas Show and Conference. https://doi.org/10.2118/198000-MS.

Aliabadian, E., Esmaeili, S., Sadeghi, S. et al 2022. New insight to polymer transport in porous media to enhance heavy oil recovery: Lab experiment and numerical simulation. *Fuel* **322**.

Alzaabi, M. A., Gausdal Jacobsen, J., Masalmeh, S.et al 2020. Polymer Injectivity Test Design Using Numerical Simulation. *Polymers (Basel)* **12** (4). https://www.ncbi.nlm.nih.gov/pubmed/32260078.

Andrew, L. C. 1998. Special Functions of Mathematics for Engineers. Oxford, Oxford University Press (Reprint).

Azad, M. S. 2022. Characterization of Nonlinear Viscoelastic Properties of Enhanced Oil Recovery Polymer Systems Using Steady-Shear Rheometry. *SPE Journal*: 1–19. https://doi.org/10.2118/212824-PA.

Azad, M. S. and Trivedi, J. J. 2019a. Novel Viscoelastic Model For Predicting the Synthetic Polymer's Viscoelastic Behavior in Porous Media Using Direct Extensional Rheological Measurements. *Fuel* **235**: 218–226.

Azad, M. S. and Trivedi, J. J. 2019b. Quantification of the Viscoelastic Effects During Polymer Flooding: A Critical Review. *SPE Journal* **24** (06): 2731–2757. https://doi.org/10.2118/195687-PA.

Azad, M. S. and Trivedi, J. J. 2020. Extensional Effects during Viscoelastic Polymer Flooding: Understanding Unresolved Challenges. *SPE Journal* **25** (04): 1827–1841. https://doi.org/10.2118/201112-PA.

Azad, M. S. and Trivedi, J. J. 2021. Quantification of Sor Reduction during Polymer Flooding Using Extensional Capillary Number. *SPE Journal* **26** (03): 1469–1498. https://doi.org/10.2118/204212-PA.

Belyadi, H., Fathi, E., and Belyadi, F. 2019. Chapter Thirteen - Rock Mechanical Properties and In-Situ Stresses. In *Hydraulic Fracturing in Unconventional Reservoirs (Second Edition)*, ed. Hoss Belyadi, *Ebrahim Fathi and Fatemeh Belyadi*, 215–231. Gulf Professional Publishing.

Biot, M. A. and Willis, D. G. 2021. The Elastic Coefficients of the Theory of Consolidation. *Journal of Applied Mechanics* **24** (4): 594–601. https://doi.org/10.1115/1.4011606.

Bird, R. B., Stewart, W. E., and Lightfoot, E. N. 2009. Transport Phenomena: Wiley.

Briscoe, B., Luckham, P., and Zhu, S. 1999. Pressure influences upon shear thickening of poly(acrylamide) solutions. *Rheologica Acta* **38** (3): 224–234. https://doi.org/10.1007/s003970050172.

Cannella, W. J., Huh, C., and Seright, R. S. 1988. Prediction of Xanthan Rheology in Porous Media. *Proc., SPE Annual Technical Conference and Exhibition*. https://doi.org/10.2118/18089-MS.

Carreau, P. J. 1972. Rheological Equations from Molecular Network Theories. *Transactions of the Society of Rheology* **16** (1): 99–127. https://doi.org/10.1122/1.549276.

Chauveteau, G. 1981. Molecular Interpretation of Several Different Properties of Flow of Coiled Polymer Solutions Through Porous Media in Oil Recovery Conditions. SPE-10060-MS. https://doi.org/10.2118/10060-MS.

Chiyu, X., Ke, X., Pengpeng, Q. et al 2022. A New Mechanism Of Viscoelastic Fluid for Enhanced Oil Recovery: Viscoelastic Oscillation. *Advances in Geo-Energy Research* **6** (3): 267–268. https://doi.org/10.46690/ager.2022.03.10.

Clemens, T., Deckers, M., Kornberger, M. et al 2013. Polymer Solution Injection - Near Wellbore Dynamics and Displacement Efficiency, Pilot Test Results, Matzen Field, Austria. Presented at the EAGE Annual Conference & Exhibition incorporating SPE Europec, London, UK. 2013/6/10/. https://doi.org/10.2118/164904-MS.

CMG, C. M. G. L. 2022. GEM Compositional & Unconventional Simulator, 2022. 10 edition (Reprint).

Cocco, M. D., Volzone, D., Fuzul, E. et al 2020. Novel Analytical Approach for Polymer Injectivity Tests in Los Perales Field, Argentina. Presented at the SPE Latin American and Caribbean Petroleum Engineering Conference, Virtual. 2020/7/20/. https://doi.org/10.2118/199071-MS.

Dandekar, A., Bai, B., Barnes, J. et al 2021. Heavy Oil Polymer EOR in the Challenging Alaskan Arctic - It Works! Presented at the SPE/AAPG/SEG Unconventional Resources Technology Conference. https://doi.org/10.15530/urtec-2021-5077.

Delamaide, E., Bazin, B., Rousseau, D. et al 2014. Chemical EOR for Heavy Oil: The Canadian Experience. Presented at the SPE EOR Conference at Oil and Gas West Asia, Muscat, Oman. 2014/3/31/. https://doi.org/10.2118/169715-MS.

Delshad, M., Kim, D. H., Magbagbeola, O. A. et al 2008. Mechanistic Interpretation and Utilization of Viscoelastic Behavior of Polymer Solutions for Improved Polymer-Flood Efficiency. Presented at the SPE Symposium on Improved Oil Recovery, Tulsa, Oklahoma, USA. 2008/1/1/. https://doi.org/10.2118/113620-MS.

Delshad, M., Pope, G. A., and Sepehrnoori, K. 1996. A compositional simulator for modeling surfactant enhanced aquifer remediation, 1 formulation. *Journal of Contaminant Hydrology* **23** (4): 303–327. https://doi.org/10.1016/0169-7722(95)00106-9.

Dupuis, G., Antignard, S., Giovannetti, B. et al 2017. A New Thermally Stable Synthetic Polymer for Harsh Conditions of Middle East Reservoirs. Part I. Thermal Stability and Injection in Carbonate Cores. Presented at the Abu Dhabi International Petroleum Exhibition & Conference. https://doi.org/10.2118/188479-MS.

Dyes, A. B., Kemp, C. E., and Caudle, B. H. 1958. Effect of Fractures on Sweep-out Pattern. *Transactions of the AIME* **213** (01): 245–249. https://doi.org/10.2118/1071-G.

Economides, M. J., Hill, A. D., and Ehlig-Economides, C. 1994. *Petroleum Production Systems*: PTR Prentice Hall.

Economides, M. J. and Nolte, K. G. 2000. *Reservoir Stimulation*: Wiley.

Ehrenfried, D. H. 2013. Impact of Viscoelastic Polymer flooding on Residual Oil Saturation in Sandstones. MS Thesis, The University of Texas at Austin, Austin, Texas (December 2013).

Erincik, M. Z., Qi, P., Balhoff, M. T. et al 2018. New Method To Reduce Residual Oil Saturation by Polymer Flooding. *SPE Journal* **23** (05): 1944–1956. https://doi.org/10.2118/187230-PA.

Friehauf, K. E., Suri, A., and Sharma, M. M. 2010. A Simple and Accurate Model for Well Productivity for Hydraulically Fractured Wells. *SPE Production & Operations* **25** (04): 453–460. https://doi.org/10.2118/119264-PA.

Gadde, P. B. and Sharma, M. M. 2001. Growing Injection Well Fractures and Their Impact on Waterflood Performance. Presented at the SPE Annual Technical Conference and Exhibition. https://doi.org/10.2118/71614-MS.

Geertsma, J. and De Klerk, F. 1969. A Rapid Method of Predicting Width and Extent of Hydraulically Induced Fractures. *Journal of Petroleum Technology* **21** (12): 1571–1581. https://doi.org/10.2118/2458-PA.

Gidley, J. L. and Engineers, S. O. P. 1989. Recent Advances in Hydraulic Fracturing: Henry L. Doherty Memorial Fund of AIME, Society of Petroleum Engineers.

Glasbergen, G., Wever, D., Keijzer, E. et al 2015. Injectivity Loss in Polymer Floods: Causes, Preventions and Mitigations. Presented at the SPE Kuwait Oil and Gas Show and Conference, Mishref, Kuwait. 2015/10/11/. https://doi.org/10.2118/175383-MS.

Gumpenberger, T., Deckers, M., Kornberger, M. et al 2012. Experiments and Simulation of the Near-Wellbore Dynamics and Displacement Efficiencies of Polymer Injection, Matzen Field, Austria. SPE-161029-MS. https://doi.org/10.2118/161029-MS.

Guo, B., Liu, X., and Tan, X. 2017. Chapter 14 - Hydraulic Fracturing. In *Petroleum Production Engineering* (Second Edition), ed. Boyun Guo, Xinghui Liu and Xuehao Tan, 389–501. Boston: Gulf Professional Publishing.

Guo, H., Song, K., Liu, S. et al 2021. Recent Advances in Polymer Flooding in China: Lessons Learned and Continuing Development. *SPE Journal* **26** (04): 2038–2052. https://doi.org/10.2118/204455-PA.

Haimson, B. and Fairhurst, C. 1967. Initiation and Extension of Hydraulic Fractures in Rocks. *Society of Petroleum Engineers Journal* **7** (03): 310–318. https://doi.org/10.2118/1710-PA.

Hassan, A. M., Al-Shalabi, E. W., and Ayoub, M. A. 2022. Updated Perceptions on Polymer-Based Enhanced Oil Recovery toward High-Temperature High-Salinity Tolerance for Successful Field Applications in Carbonate Reservoirs. *Polymers* **14** (10). https://doi.org/10.3390/polym14102001.

Heemskerk, J., Rosmalen, R., Janssen-van, R. et al 1984. Quantification of Viscoelastic Effects of Polyacrylamide Solutions. Presented at the SPE Enhanced Oil Recovery Symposium. https://doi.org/10.2118/12652-MS.

Hincapie, R. E., Rock, A., Wegner, J.et al 2017. Oil Mobilization by Viscoelastic Flow Instabilities Effects during Polymer EOR: A Pore-Scale Visualization Approach. Proc., SPE Latin America and Caribbean Petroleum Engineering Conference. https://doi.org/10.2118/185489-MS.

Hirasaki, G. J. and Pope, G. A. 1974. Analysis of Factors Influencing Mobility and Adsorption in the Flow of Polymer Solution Through Porous Media. *Society of Petroleum Engineers Journal* **14** (04): 337–346. https://doi.org/10.2118/4026-PA.

Howe, A. M., Clarke, A., and Giernalczyk, D. 2015. Flow of concentrated viscoelastic polymer solutions in porous media: effect of M(W) and concentration on elastic turbulence onset in various geometries. *Soft Matter* **11** (32): 6419–6431. https://doi.org/10.1039/c5sm01042j.

Hwang, J., Sharma, M., Chiotoroiu, M.-M.et al 2019. Viscoelastic Polymer Injectivity: A Novel Semi-Analytical Simulation Approach and Impact of Induced Fractures and Horizontal Wells. Presented at the SPE Annual Technical Conference and Exhibition, Calgary, Alberta, Canada. 2019/9/23/. https://doi.org/10.2118/195978-MS.

Hwang, J. and Sharma, M. M. 2013. A 3-Dimensional Fracture Propagation Model for Long-Term Water Injection. Presented at the 47th US Rock Mechanics/Geomechanics Symposium.

Hwang, J., Zheng, S., Sharma, M. et al 2022. Use of Horizontal Injectors for Improving Injectivity and Conformance in Polymer Floods. Presented at the SPE Improved Oil Recovery Conference. https://doi.org/10.2118/209373-MS.

Jiang, B., Keffer, D. J., Edwards, B. J. et al 2003. Modeling shear thickening in dilute polymer solutions: Temperature, concentration, and molecular weight dependencies. *Journal of Applied Polymer Science* **90** (11): 2997–3011. https://onlinelibrary.wiley.com/doi/abs/10.1002/app.12950.

Jin, J., Qi, P., Mohanty, K. et al 2020. Experimental Investigation of the Effect of Polymer Viscoelasticity on Residual Saturation of Low Viscosity Oils. Presented at the SPE *Improved Oil Recovery Conference*. https://doi.org/10.2118/200414-MS.

Kim, D. H., Lee, S., Ahn, C. H. et al 2010. Development of a Viscoelastic Property Database for EOR Polymers. Presented at the SPE Improved Oil Recovery Symposium, Tulsa, Oklahoma, USA. 2010/1/1/. https://doi.org/10.2118/129971-MS.

Koh, H. 2015. *Experimental Investigation of the Effect of Polymers on Residual Oil Saturation.* PhD dissertation, The University of Texas at Austin, Austin, Texas (January 2015).

Koh, H., Lee, V. B., and Pope, G. A. 2018. Experimental Investigation of the Effect of Polymers on Residual Oil Saturation. *SPE Journal* **23** (01): 1–17. https://doi.org/10.2118/179683-PA.

Lake, L. W., Johns, R., Rossen, W. R.et al 2014. Fundementals of Enhanced Oil Recovery: Society of Petroleum Engineers.

Lee, K. 2012. Impact of Fracture Creation and Growth on Well Injectivity and Reservoir Sweep During Waterflooding and Chemical Eor Processes. Doctor of Philosophy, University of Texas at Austin, Austin, Texas (May 2012). http://hdl.handle.net/2152/ETD-UT-2012-05-5061.

Li, Z., Espinoza, D. N., and Balhoff, M. T. 2022. Simulation of Polymer Injection in Granular Media: Implications of Fluid-Driven Fractures, Water Quality, and Undissolved Polymers on Polymer Injectivity. *SPE Journal*: 1–12. https://doi.org/10.2118/200412-PA.

Li, Z., Luo, H., Bhardwaj, P.et al 2016. Modeling Dynamic Fracture Growth Induced by Non-Newtonian Polymer Injection. *Journal of Petroleum Science and Engineering* **147**: 395–407. https://www.sciencedirect.com/science/article/pii/S0920410516303503.

Liu, Z.-x., Liang, Y., Wang, Q.et al 2020. Status and Progress of Worldwide EOR Field Applications. *Journal of Petroleum Science and Engineering* **193**.

Lohne, A., Nødland, O., Stavland, A.et al 2017. A model for non-Newtonian flow in porous media at different flow regimes. *Computational Geosciences* **21**: 1–24. https://doi.org/10.1007/s10596-017-9692-6.

Lotfollahi, M., Farajzadeh, R., Delshad, M.et al 2015. Mechanistic Simulation of Polymer Injectivity in Field Tests. Presented at the SPE Asia Pacific Enhanced Oil Recovery Conference, Kuala Lumpur, Malaysia. 2015/8/11/. https://doi.org/10.2118/174665-MS.

Lotfollahi, M., Koh, H., Li, Z. et al 2016. Mechanistic Simulation of Residual Oil Saturation in Viscoelastic Polymer Floods. Presented at the SPE EOR Conference at Oil and Gas West Asia. https://doi.org/10.2118/179844-MS.

Ma, Y. 2015. Diagnosis of Induced Hydraulic Fractures during Polymer Injection. MS Thesis, The University of Texas at Austin.

Ma, Y. and McClure, M. W. 2017. The Effect of Polymer Rheology and Induced Fracturing on Injectivity and Pressure-Transient Behavior. *SPE Reservoir Evaluation & Engineering* **20** (02): 394–402. https://doi.org/10.2118/184389-PA.

Manichand, R. N. N., Moe Soe Let, K. P. P., Gil, L. et al 2013. Effective Propagation of HPAM Solutions Through the Tambaredjo Reservoir During a Polymer Flood. *SPE Production & Operations* **28** (04): 358–368. https://doi.org/10.2118/164121-PA.

McClure, M. W. 2012. Modeling and Characterization of Hydraulic Stimulation and Induced Seismicity in Geothermal and Shale Gas Reservoirs. Phd, Stanford University (December 2012).

Melo, M. A., Lins, A. G., and Silva, I. P. G. 2017. Lessons Learned From Polymer Flooding Pilots in Brazil. Presented at the SPE Latin America and Caribbean Mature Fields Symposium, Salvador, Bahia, Brazil. 2017/3/15/. https://doi.org/10.2118/184941-MS.

Mirzaie Yegane, M., Boukany, P. E., and Zitha, P. 2022. Fundamentals and Recent Progress in the Flow of Water-Soluble Polymers in Porous Media for Enhanced Oil Recovery. *Energies* **15** (22).

Miskimins, J. L. 2019. Hydraulic Fracturing: Fundamentals and Advancements: Society of Petroleum Engineers.

Mohamed, A. I. A., Khishvand, M., and Piri, M. 2023. The role of injection fluid elasticity in microscopic displacement efficiency of residual non-wetting phase: An in-situ experimental investigation. *Fuel* **333**.

Nordgren, R. P. 1972. Propagation of a Vertical Hydraulic Fracture. *Society of Petroleum Engineers Journal* **12** (04): 306–314. https://doi.org/10.2118/3009-PA.

Pan, G., Zhang, L., Huang, J. et al 2020. Twelve Years Field Applications of Offshore Heavy Oil Polymer Flooding from Continuous Injection to Alternate Injection of Polymer-Water. https://doi.org/10.4043/30277-MS.

Paul, B. 1968. Generalized pyramidal fracture and yield criteria. *International Journal of Solids and Structures* **4** (2): 175–196.

Peaceman, D. W. 1978. Interpretation of Well-Block Pressures in Numerical Reservoir Simulation(includes associated paper 6988). *Society of Petroleum Engineers Journal* **18** (03): 183–194. https://doi.org/10.2118/6893-PA.

Prats, M. 1961. Effect of Vertical Fractures on Reservoir Behavior-Incompressible Fluid Case. *Society of Petroleum Engineers Journal* **1** (02): 105–118. https://doi.org/10.2118/1575-G.

Qi, P. 2018. The effect of polymer viscoelasticity on residual oil saturation. Doctoral, The University of Texas at Austin (2018-06-13). http://hdl.handle.net/2152/67953.

Qi, P., Ehrenfried, D. H., Koh, H. et al 2017. Reduction of Residual Oil Saturation in Sandstone Cores by Use of Viscoelastic Polymers. *SPE Journal* **22** (02): 447–458. https://doi.org/10.2118/179689-PA.

Qi, P., Lashgari, H., Luo, H. et al 2018. Simulation of Viscoelastic Polymer Flooding - From the Lab to the Field. Presented at the SPE Annual Technical Conference and Exhibition, Dallas, Texas, USA. 2018/9/24/. https://doi.org/10.2118/191498-MS.

Quosay, A. A., Knez, D., and Ziaja, J. 2020. Hydraulic Fracturing: New Uncertainty Based Modeling Approach for Process Design Using Monte Carlo Simulation Technique. *PLOS ONE* **15** (7): e0236726. https://doi.org/10.1371/journal.pone.0236726.

Rahman, M. M. and Rahman, M. K. 2010. A Review of Hydraulic Fracture Models and Development of an Improved Pseudo-3D Model for Stimulating Tight Oil/Gas Sand. *Energy Sources, Part A: Recovery, Utilization, and Environmental Effects* **32** (15): 1416–1436. https://doi.org/10.1080/15567030903060523.

Rashid, B., Stapley, J., Clifford, P.et al 2018. Successful Field Trial of a Novel, Reservoir-Triggered Polymer: Results, Interpretation and Simulation. Presented at the SPE Improved Oil Recovery Conference, Tulsa, Oklahoma, USA. 2018/4/14/. https://doi.org/10.2118/190159-MS.

Rock, A., Hincapie, R. E., Tahir, M.et al 2020. On the Role of Polymer Viscoelasticity in Enhanced Oil Recovery: Extensive Laboratory Data and Review (in eng). *Polymers (Basel)* **12** (10).

Sagyndikov, M. S., Kushekov, R. M., and Seright, R. S. 2022. Review of Important Aspects and Performances of Polymer Flooding versus ASP Flooding. *Bulletin of the Karaganda University "Chemistry" series*.

Sarvaramini, E. and Garagash, D. 2015. Breakdown of a Pressurized Fingerlike Crack in a Permeable Solid. *Journal of Applied Mechanics* **82**: 061006.

Seright, R. S. 1983. The Effects of Mechanical Degradation and Viscoelastic Behavior on Injectivity of Polyacrylamide Solutions. *Society of Petroleum Engineers Journal* **23** (03): 475–485. https://doi.org/10.2118/9297-PA.

Seright, R. S. 2017. How Much Polymer Should Be Injected During a Polymer Flood? Review of Previous and Current Practices. *SPE Journal* **22** (01): 1–18. https://doi.org/10.2118/179543-PA.

Seright, R. S., Azad, M. S., Abdullah, M. B.et al 2023. Effect of Residual Oil Saturation and Salinity on HPAM Rheology in Porous Media. Proc., SPE Annual Technical Conference and Exhibition.

Seright, R. S., Seheult, J. M., and Talashek, T. 2009. Injectivity Characteristics of EOR Polymers. *SPE Reservoir Evaluation & Engineering* **12** (05): 783–792. https://doi.org/10.2118/115142-PA.

Seright, R. S., Wang, D., Lerner, N.et al 2018. Can 25-cp Polymer Solution Efficiently Displace 1,600-cp Oil During Polymer Flooding? *SPE Journal* **23** (06): 2260–2278. https://doi.org/10.2118/190321-PA.

Seright, R. S., Wavrik, K. E., Zhang, G. et al 2021. Stability and Behavior in Carbonate Cores for New Enhanced-Oil-Recovery Polymers at Elevated Temperatures in Hard Saline Brines. *SPE Reservoir Evaluation & Engineering* **24** (01): 1–18. https://doi.org/10.2118/200324-PA.

Shankar, V. and Sharma, G. 2022. Decoding the Impact of Injection-Induced Fractures on the Sweep Efficiency of a Mature Polymer Flood through Pressure Falloff Analysis. *SPE Reservoir Evaluation & Engineering*: 1–17. https://doi.org/10.2118/212825-PA.

Sheng, J. J. 2011. Chapter 5 - Polymer Flooding. In *Modern Chemical Enhanced Oil Recovery*, ed. James J. Sheng, 101–206. Boston: Gulf Professional Publishing.

Sheng, J. J. 2013. *Enhanced Oil Recovery Field Case Studies*.

Skauge, A., Zamani, N., Gausdal Jacobsen, J.et al 2018. Polymer Flow in Porous Media: Relevance to Enhanced Oil Recovery. *Colloids and Interfaces* **2** (3): 27. https://www.mdpi.com/2504-5377/2/3/27.

Skauge, T., Ormehaug, P. A., Alsumaiti, A.et al 2022. Polymer Stability at Harsh Temperature and Salinity Conditions. Presented at the SPE Conference at Oman Petroleum & Energy Show. https://doi.org/10.2118/200178-MS.

Smith, M. B. and Montgomery, C. 2015. Hydraulic Fracturing: CRC Press.

SNF-FLORGER. 2012.Enhancing Polymer Flooding Performance, 32. France (Reprint). https://www.biotex-malaysia.com/wp-content/uploads/2015/07/Oil-30-Years-of-EOR.pdf.

Sorbie, K. S. 1990. Polymer-Improved Oil Recovery. USA: Springer Science & Business Media.

Standnes, D. C. and Skjevrak, I. 2014. Literature Review of Implemented Polymer Field Projects. *Journal of Petroleum Science and Engineering* **122**: 761–775. https://doi.org/10.1016/j.petrol.2014.08.024.

Suri, A. and Sharma, M. M. 2009. Fracture Growth in Horizontal Injectors. Presented at the SPE Hydraulic Fracturing Technology Conference, The Woodlands, Texas. 2009/1/1/. https://doi.org/10.2118/119379-MS.

Suri, A., Sharma, M. M., and Peters, E. J. 2011. Estimates of Fracture Lengths in an Injection Well by History Matching Bottomhole Pressures and Injection Profile. *SPE Reservoir Evaluation & Engineering* **14** (04): 385–397. https://doi.org/10.2118/132524-PA.

Taber, J. J., Martin, F. D., and Seright, R. S. 1997. EOR Screening Criteria Revisited - Part 1: Introduction to Screening Criteria and Enhanced Recovery Field Projects. *SPE Reservoir Engineering* **12** (03): 189–198. https://doi.org/10.2118/35385-PA.

Teng, B., Li, H., and Yu, H. 2020. A Novel Analytical Fracture-Permeability Model Dependent on Both Fracture Width and Proppant-Pack Properties. *SPE Journal* **25** (06): 3031–3050. https://doi.org/10.2118/201093-PA.

Tran, D., Buchanan, L., and Nghiem, L. 2008. Improved Gridding Technique for Coupling Geomechanics to Reservoir Flow. Proc., SPE Annual Technical Conference and Exhibition. https://doi.org/10.2118/115514-MS.

Tran, D., Settari, A., and Nghiem, L. 2012. Initiation And Propagation of Secondary Cracks In Thermo-Poroelastic Media. Proc., 46th US Rock Mechanics/Geomechanics Symposium.

Tran, D., Settari, A., and Nghiem, L. 2013. Effects of Thermally-Induced Secondary Cracks on Hydraulic Fracture Geometry. Proc., SPE Unconventional Resources Conference Canada. https://doi.org/10.2118/167123-MS.

Valko, P. P. and Economides, M. J. 1995. Hydraulic fracture mechanics.

Vongvuthipornchai, S. and Raghavan, R. 1987. Pressure Falloff Behavior in Vertically Fractured Wells: Non-Newtonian Power-Law Fluids. *SPE Formation Evaluation* **2** (04): 573–589. https://doi.org/10.2118/13058-PA.

Wang, D., Han, P., Shao, Z.et al 2008. Sweep-Improvement Options for the Daqing Oil Field. *SPE Reservoir Evaluation & Engineering* **11** (01): 18–26. https://doi.org/10.2118/99441-PA.

Wang, D., Xia, H., Yang, S.et al 2010. The Influence of Visco-Elasticity on Micro Forces and Displacement Efficiency in Pores, Cores and in the Field. Presented at the SPE EOR Conference at Oil & Gas West Asia. https://doi.org/10.2118/127453-MS.

Wu, X., Wang, Y., Al Naabi, A. et al 2019. A New Polymer Flooding Technology for Improving Low Permeability Carbonate Reservoir Recovery--From Lab Study to Pilot Test--Case Study from Oman. Presented at the Abu Dhabi International Petroleum Exhibition & Conference. https://doi.org/10.2118/197912-MS.

Wu, Z., Cui, C., Jia, P. et al 2022. Advances and Challenges in Hydraulic Fracturing of Tight Reservoirs: A Critical Review. *Energy Geoscience* **3** (4): 427–435. https://doi.org/10.1016/j.engeos.2021.08.002.

Zechner, M., Buchgraber, M., Clemens, T. et al 2013. Flow of Polyacrylamide Polymers in the Near-Wellbore-Region, Rheological Behavior within Induced Fractures and Near-Wellbore Area. Presented at the SPE Annual Technical Conference and Exhibition. https://doi.org/10.2118/166085-MS.

Zechner, M., Clemens, T., Suri, A. et al 2015. Simulation of Polymer Injection Under Fracturing Conditions—An Injectivity Pilot in the Matzen Field, Austria. *SPE Reservoir Evaluation & Engineering* **18** (02): 236–249. https://doi.org/10.2118/169043-PA.

Zeynalli, M., Al-Shalabi, E. W., and AlAmeri, W. 2021. Core-to-Field-Scale Simulations of Polymer Viscoelastic Effect on Oil Recovery Using the Extended Viscoelastic Model. Presented at the Abu Dhabi International Petroleum Exhibition & Conference. https://doi.org/10.2118/208168-MS.

Zeynalli, M., Al-Shalabi, E. W., and AlAmeri, W. 2022. An Extended Unified Viscoelastic Model for Predicting Polymer Apparent Viscosity at Different Shear Rates. *SPE Reservoir Evaluation & Engineering*: 1–23. https://doi.org/10.2118/206010-PA.

Zhang, J. and Yin, S.-X. 2017. Fracture Gradient Prediction: An Overview and An Improved Method. *Petroleum Science* **14** (4): 720–730.

Zhang, J. J. 2019. Chapter 2 - Rock Physical and Mechanical Properties. In *Applied Petroleum Geomechanics*, ed. Jon Jincai Zhang, 29–83. Gulf Professional Publishing.

Zoback, M. D. 2010. Reservoir Geomechanics: Cambridge University Press.

Appendix A

The effective shear rate $\dot{\gamma}_{eff}$ (sec^{-1}) in the reservoir is given by (Cannella et al. 1988).

$$\dot{\gamma}_{\text{eff}} = \left[\frac{3n+1}{4n}\right]^{\frac{n}{n-1}} \left[\frac{4CU_r}{\sqrt{8kk_{rw}S_w\phi}}\right], \tag{24}$$

where n is the shear-thinning exponent. C is a correction factor that converts bulk polymer viscosity measured in the viscometer into insitu polymer rheology. C is measured in the lab as a function of rock porosity, permeability, and polymer rheology (Sorbie 1990). Cannella et al. (1988) showed that for a permeability range of 10's to 100's mD, $C = 6$ is a reasonable value for Xanthan gum biopolymer. Koh et al. (2018) found $C = 4$ can fit accurately a permeability range of ~100 – 1000 mD for HPAM polymers: FP-3630 and FP-3330. The Darcy velocity U_r (m/s) for radial flow as

$$U_r = \frac{k_p}{\mu_{\text{app}}}\frac{dP_p}{dr}, \tag{25}$$

where, μ_{app} (cp) is the apparent viscosity, k_p (m^2) is the polymer permeability, dP_p is the polymer pressure drop (psi), r (m) is the polymer slug radius. The polymer permeability can be calculated from the permeability reduction equation

$$k_p = \frac{k_w}{R_k} = \frac{kk_{rw}}{R_k}, \tag{26}$$

with k (m^2), k_w, k_{rw} and R_k being the reservoir permeability, water permeability, water endpoint relative permeability, and permeability reduction factor, respectively.

To simplify our calculations, let us denote

$$A = \frac{4}{\sqrt{8}}\left[\frac{3n+1}{4n}\right]^{\frac{n}{n-1}} \qquad \text{and} \qquad B = \frac{C}{\sqrt{kk_{rw}S_w\phi}}. \tag{27}$$

This simplifies the effective shear rate expression to

$$\dot{\gamma}_{\text{eff}} = ABU_r, \tag{28}$$

where the apparent polymer viscosity becomes

$$\mu_{\text{app}} = \mu_\infty + \left(\mu_p^0 - \mu_w\right)\left[1 + (\lambda ABU_r)^2\right]^{\frac{n-1}{2}} + \mu_{\text{max}}\left[1 - \exp\left(-\left(\lambda_2 \tau ABU_r\right)^{n_2 - 1}\right)\right]. \tag{29}$$

Appendix B

The maximum fracture net pressure and width from Li et al. (2016) for KGD model are presented here. The maximum net pressure at the wellbore ($p_{net(\max)}$) is

$$p_{net(\max)-KGD} = \left[\left(\frac{q_i}{\mathrm{h_f}}\frac{2n+1}{n}\right)^n \left(4KC_{Turb}L_f\right)\left(\frac{E'}{4L_f}\right)^{2n+1}\right]^{\frac{1}{2n+2}}. \tag{30}$$

The maximum fracture width at the wellbore for KGD model is

$$w_{f\max-KGD} = \left(\frac{4L_f}{E'}\right)\left[\left(\frac{q_i}{\mathrm{h_f}}\frac{2n+1}{n}\right)^n \left(4KC_{Turb}L_f\right)\left(\frac{E'}{4L_f}\right)^{2n+1}\right]^{\frac{1}{2n+2}}, \tag{31}$$

where the average fracture width w¯f=(π/4)wf max−KGD (Valko and Economides 1995, Rahman and Rahman 2010).

Appendix C

Here we will derive the fracture pressure and geometry for a power-law non-Newtonian fluid (polymer) in a PKN model, similar to Li et al. (2016) derivation approach that is based on KGD model. The fracture rate for the narrow slit model (Bird et al. 2009):

$$q_f = \frac{AB}{2+\frac{1}{n}}\left(\left|\frac{\Delta P}{\Delta L}\right|\frac{B}{K}\right)^{\frac{1}{n}}, \tag{32}$$

where K is the power law parameter in $cp.s^{(n-1)}$, n is the power-law exponent, B=wf2, and for PKN model A=Area=14hfwf then,

$$q_f = \frac{\mathrm{h_f}\frac{w_f 2}{8}}{2+\frac{1}{n}}\left(\left|\frac{\Delta P}{\Delta L}\right|\frac{w_f}{2K}\right)^{\frac{1}{n}}, \tag{33}$$

$$\frac{dp_f}{dx} = 2K\left[\frac{8q_f\left(2+\frac{1}{n}\right)}{\pi\mathrm{h_f}}\right]^n\left(\frac{1}{w_f}\right)^{2n+1}. \tag{34}$$

Suri and Sharma (2009) proposed that a uniform average leak-off rate from the fracture faces results in a fracture flow rate qf=12qi(1−xfLf). To account for turbulence impact, a turbulence correction factor C_{Tur}= = 16 / 3π for turbulence flow and a value of unity for laminar flow is added (Perkins and Kern (1961)). By including the uniform average leakoff rate assumption and turbulence correction factor in Eq. (34):

$$\frac{dp_f}{dx} = -2C_{Turb}K\left[\frac{4q_i\left(1-\frac{x_f}{L_f}\right)\left(2+\frac{1}{n}\right)}{\pi\mathrm{h_f}}\right]^n\left(\frac{1}{w_f}\right)^{2n+1}. \tag{35}$$

Integrating,

$$\int_{pnet@xf=0}^{pnet@xf=tip}\left(w_f\right)^{2n+1}dp_f = -2C_{Turb}K\left[\frac{4q_i\left(2+\frac{1}{n}\right)}{\pi\mathrm{h_f}}\right]^n\int_0^{x_f}\left(1-\frac{x_f}{L_f}\right)^n dx. \tag{36}$$

The fracture width for PKN model is calculated as (Gidley and Engineers 1989),

$$w_f(x,t) = \frac{2h_f\left(p_f(x)-\sigma_H\right)}{E'} = \frac{2h_f p_{net}(x)}{E'}, \tag{37}$$

where E'=E1−v2 and pnet(xf)=(pf(xf)−σh min). Substituting Eq.(37) in Eq.(36),

$$\left(\frac{2h_f}{E'}\right)^{2n+1}\int\left(p_{net}(x_f)\right)^{2n+1}dp_{net} = -2C_{Turb}K\left[\frac{4q_i\left(\frac{2n+1}{n}\right)}{\pi\mathrm{h_f}}\right]^n\int\left(1-\frac{x_f}{L_f}\right)^n dx. \tag{38}$$

Integrating and assuming that at the fracture tip the net pressure $p_{net}(x_f) = (p_f(x) - \sigma_H)$ is zero where $x_f = L_f$.

$$\left(\frac{2h_f}{E'}\right)^{2n+1}\frac{\left[p_{net}(x_f)\right]^{2n+2}}{2n+2} = \left[\frac{4q_i\left(\frac{2n+1}{n}\right)}{\pi\mathrm{h_f}}\right]^n\left(\frac{2C_{Turb}L_f K}{n+1}\right)\left(1-\frac{x_f}{L_f}\right)^{n+1}, \tag{39}$$

$$\left[p_{net}(x_f)\right]^{2n+2} = \left(\frac{E'}{2h_f}\right)^{2n+1}\left[\frac{4q_i\left(\frac{2n+1}{n}\right)}{\pi\mathrm{h_f}}\right]^n\left(4C_{Turb}L_f K\right)\left(1-\frac{x_f}{L_f}\right)^{n+1}, \tag{40}$$

$$p_{net}(x_f)=\left\{\left(\frac{E'}{2h_f}\right)^{2n+1}\left[\frac{4q_i\left(\frac{2n+1}{n}\right)}{\pi \mathrm{h_f}}\right]^n\left(4C_{Turb}L_fK\right)\left(1-\frac{x_f}{L_f}\right)^{n+1}\right\}^{\frac{1}{2n+2}}, \tag{41}$$

From substituting Eq. (41) in Eq. (37), the fracture width is

$$w_f(x_f)=\left(\frac{2h_f}{E'}\right)\left\{\left(\frac{E'}{2h_f}\right)^{2n+1}\left[\frac{4q_i\left(\frac{2n+1}{n}\right)}{\pi \mathrm{h_f}}\right]^n\left(4C_{Turb}L_fK\right)\left(1-\frac{x_f}{L_f}\right)^{n+1}\right\}^{\frac{1}{2n+2}}. \tag{42}$$

The maximum net pressure at wellbore where $x_f = 0$ is

$$p_{net}(0)=p_{net(\max)}=\left\{\left(\frac{E'}{2h_f}\right)^{2n+1}\left[\frac{4q_i\left(\frac{2n+1}{n}\right)}{\pi \mathrm{h_f}}\right]^n\left(4C_{Turb}L_fK\right)\right\}^{\frac{1}{2n+2}}. \tag{43}$$

Since $p_{net} = p_f - \sigma_{h\,\min}$, then the fracture pressure at the wellbore is

$$p_f = p_{net(\max)} + \sigma_{h\min}. \tag{44}$$

Similarly, the maximum width at wellbore where $x_f = 0$ is

$$w_f(0)=w_{f\max}=\left(\frac{2h_f}{E'}\right)\left\{\left(\frac{E'}{2h_f}\right)^{2n+1}\left[\frac{2q_i\left(\frac{2n+1}{n}\right)}{\pi \mathrm{h_f}}\right]^n\left(4C_{Turb}L_fK\right)\right\}^{\frac{1}{2n+2}}, \tag{45}$$

where the average fracture width w¯f=(π/5)wfmax for PKN model (Valko and Economides 1995, Rahman and Rahman 2010).

Appendix D

The lab and reservoir properties used in the Results and Discussion section case studies are provided in this appendix.

Table D-1—Physical parameters used for verifying the UVIM with Ma and McClure (2017) model

Parameter	Value	Parameter	Value
Injection rate (q), bbls/day	2200	Zero-shear rate polymer viscosity, cp	33.84
Permeability (k), mD	300	Time constant (λ), sec	0.792
Formation thickness (h), ft	65	Shear-thickening exponent (n_2)	3.5
Wellbore radius (r_w), ft	0.35*	Ap_{11}, Ap_{22}	3.5, 21.76
Drainage radius (r_e), ft	738	Maximum polymer viscosity in shear-thickening (μ_{max}), cp	16
Boundary pressure (P_e), psi	2610	Shear-thinning parameter (λ_2)	0.01
Porosity (ϕ), %	22	τ_0, τ_1	0.01, 0.3
Water saturation (S_w), %	100	Insitu relaxation time (τ), sec	0.068
Water endpoint relative permeability (k_{rwo})	1	Minimum horizontal stress, psi	3770
Water viscosity (μ_w), cp	1	Maximum horizontal stress, psi	NA
Permeability reduction factor	1	Fracture initiation pressure (p_{fi})	3770
Polymer concentration, wt% (C_p)	0.2	Power law exponent, n_p	0.8
Effective salinity (C_{SEP}), meq/mL	0.051	Power law parameter (K), cp.sec$^{(n-1)}$	31
Polymer viscosity at high shear rate (μ_∞), cp	Water viscosity (1)	Young's Modulus ('E), psi	5,438,925**
Correction factor	6	Poisson's ratio (v)	0.25**
Salinity dependence slope (S_p)	0	Fracture thickness (h_f), ft	65
Ap_1, A_{P2}, A_{P3}	35, 435, 1055	Turbulence parameter (C_{turb})	1.7
Time constant paramters (BETAV1, BETAV2)	0.0192, 18.6	Critical stress intensity factor (K_{IC}),, psi.inch$^{0.5}$	0
Carreau shear thinning index (n_1)	0.78		

*

we used a value from the original simulator development study (McClure 2012), which obeys Peaceman (1978) 's condition as $r_w < 0.2\ \Delta x$.

**

from Table 4-1 in Ma (2015).

Table D-2—Physical parameters used for verifying the UVIM with UTWID model presented by Li et al. (2016)

Parameter	Value	Parameter	Value
Injection rate (q), bbls/day	356	Zero-shear rate polymer viscosity (cp)	15.64
Permeability (k), mD	100	Time constant (λ), sec	0.313
Formation thickness (h), ft	40	Shear-thickening exponent (n_2)	3.5
Wellbore radius (r_w), ft	0.25	Shear thickening parameters (Ap_{11}, Ap_{22})	2.74, 17.12
Drainage radius (r_e), ft	1500	Maximum polymer viscosity in shear-thickening (μ_{max}), cp	9.51
Boundary pressure (P_e), psi	3000	Shear-thinning parameter (λ_2)	0.01
Porosity (ϕ), %	20	τ_0, τ_1	0.3, 0.00891
Water saturation (S_w), %	70	Insitu relaxation time (τ), sec	0.3
Water endpoint relative permeability (k_{rwo})	0.3	Minimum horizontal stress, psi	4000
Water Viscosity (μ_w), cp	0.798	Maximum horizontal stress, psi	4500

Parameter	Value	Parameter	Value
Permeability reduction factor (R_k)	1	Fracture initiation pressure (p_{fi})	5000
Polymer concentration (C_p), wt%	0.15	Power law exponent, n_p	0.75
Effective salinity (C_{SEP}), meq/mL	0.051	Power law parameter (K), cp.sec$^{(n-1)}$	23.3
Polymer viscosity at high shear rate (μ_∞), cp	Water viscosity (0.798)	Young's Modulus ('E), psi	3,950,000
Shear rate correction factor (C)	6	Poisson's ratio (v)	0.3
Salinity dependence slope (S_p)	0	Fracture thickness (h_f), ft	40
Polymer viscosity parameters (Ap_1, A_{P2}, A_{P3})	35, 435, 1055	Turbulence parameter (C_{turb})	1.7
Time constant paramters (BETAV1, BETAV2)	0.0192, 18.6	Critical stress intensity factor (K_{IC}),, psi.inch$^{0.5}$	500
Carreau shear thinning index (n_1)	0.78		

Table D-3—UVIM-PKN model parameters used in CMG-GEM radial and cartesian models verification

Parameter	Value	Parameter	Value
Injection rate (q), bbl/day	1000	Zero-shear rate polymer viscosity, cp	14.16
Permeability (k), mD	250	Time constant (λ), sec	0.241
Formation thickness (h), ft	37	Shear-thickening exponent (n_2)	3.5
Wellbore radius (r_w), ft	0.4	Maximum polymer viscosity in shear-thickening (μ_{max}), cp	10
Drainage radius (r_e), ft	267	Shear-thinning parameter (λ_2)	0.01
Boundary Pressure (P_e), psi	2000	Relaxation time (τ), sec	0.05
Porosity (ϕ),%	0.22	Minimum horizontal stress, psi	2875
Water saturation (S_w), %	70	Maximum horizontal stress, psi	2875
Water endpoint relative permeability (k_{rwo})	0.3	Fracture initiation pressure (p_{fi})	3833
Water Viscosity (μ_w), cp	0.86	Power law exponent, n_p	0.773
Permeability reduction factor (R_k)	1	Power law paramter (K), cp.sec$^{(n-1)}$	19
Polymer concentration (C_p), wt%	0.136	Young's Modulus (‘E), psi	1,060,000
Effective salinity (C_{SEP}), meq/mL	0.051	Poisson's ratio (v)	0.3
Polymer viscosity at high shear rate (μ_∞), cp	0.86	Fracture thickness (h_f), ft	37
Shear rate correction factor ©	5	Turbulence parameter (C_{turb})	1.7
Salinity dependence slope (S_p)	0	Critical stress intensity factor (K_{IC}),, psi.inch$^{0.5}$	0
Carreau shear thinning index (n_1)	0.78		

Table D-4—Tabulated viscoelastic viscosity used in CMG-GEM model verification. Note the conventional shear rate unit is s^{-1}, but it is reported here in day^{-1} to match CMG-GEM simulation input format.

Shear rate (day^{-1})	Viscosity (cp)
8640	14.2
17300	14.2
43200	14.1
86400	14.1
173000	13.9
346000	13.2
605000	12.3

Shear rate (day^{-1})	Viscosity (cp)
1300000	10.8
2590000	9.45
4320000	8.54
8640000	7.47
13000000	6.91
17300000	6.56
25900000	6.13
43200000	5.8
60500000	5.85
69100000	5.98
77800000	6.18
95000000	6.73
130000000	8.3
173000000	10.5
259000000	13.3
302000000	13.7
346000000	13.8
432000000	13.7
605000000	13.5
864000000	13.3

Table D-5—CMG-GEM reservoir, fluid, and geomechanics parameters used in cartesian gridding sensitivity and the tuned 3ft×3ft grid model (CMG 2022)

Parameter	Value
$N_x \times N_y \times N_z$	157×157×1
$\Delta_x \times \Delta_y \times \Delta_z$, ft	3×3×37
Matrix permeability (kx=ky=kz), mD	250
Matrix porosity (ϕ),%	0.22
Fracture permeability (kx=ky=kz), mD	0.001
Fracture porosity (ϕ),%	0.1
Rock compressibility, psi^{-1}	3.00E-06
Water compressibility, psi^{-1}	2.00E-06
Oil and water Corey exponents (oil-water curve)	2, 2
Oil and gas Corey exponents (oil-gas curve)	6.3, 2.1
Water saturation (s_w), %	70
Oil and water endpoint relative permeability	0.7, 0.3
Oil and gas endpoint relative permeability	0.7, 0.43
Water viscosity (μ_w), cp	0.86
Oil viscsoity, cp	6
Oil density, lb/ft^3	60.222
Oil compressibility (STD conditions), psi^{-1}	1.35E-6
SHEAR FAC	4.2
Polymer molecular weight, g/mol	18

Parameter	Value
VSMIXENDP	0, 0.00136151
VSMIXFUN	0, 0.1, 0.2, 0.3, 0.4, 0.5, 0.6, 0.7, 0.8, 0.9, 1
Injection rate (q), bbl/day	1000
Polymer concentration	0.136 wt% = 0.0757 mol/kg
Wellbore radius (r_w), ft	0.4
Initial pressure (P_i), psi	2000
Boundary pressure (P_e), psi	2000
Initial minimum horizontal stress, psi	2875
Initial maximum horizontal stress, psi	2875
Initial vertical stress, psi	4000
Young's modulus ('E), psi	1060000
Poisson's ratio (v)	0.3
*GCRITICAL *TENFRAC	2000

Table D-6—Physical parameters used for the Matzen field case study (Clemens et al. 2013, Zechner et al. 2013, Zechner et al. 2015, Hwang et al. 2019)

Parameter	Value	Parameter	Value
Injection rate (q), bbls/day	2400	Zero-shear rate polymer viscosity, cp	7.8
Permeability (k), mD	550	Time constant (λ), sec	0.65
Formation thickness (h), ft	16.5	Shear-thickening exponent (n_2)	2
Wellbore radius (r_w), ft	0.3	Maximum polymer viscosity in shear-thickening (μ_{max}), cp	33
Drainage radius (r_e), ft	984	Shear-thinning parameter (λ_2)	0.01
Boundary pressure (P_e), psi	1552	Insitu relaxation time (τ), sec	0.6
Porosity (ϕ), %	26	Minimum horizontal stress, psi	2650
Water saturation (s_w), %	87	Maximum horizontal stress, psi	NA
Water endpoint relative permeability (k_{rwo})	0.3	Fracture initiation pressure (p_{fi}), psi	2650
Water viscosity (μ_w), cp	0.6	Power law exponent, n_p	0.85
Permeability reduction factor (R_K)	1	Power law parameter (K), cp.sec$^{(n-1)}$	7
Polymer concentration, wt% (C_p)	0.1	Young's Modulus ('E), psi	1,060,000
Effective salinity (C_{SEP}), meq/mL	0.051	Poisson's ratio (v)	0.365
Polymer viscosity at high shear rate (μ_∞), cp	0.6	Fracture thickness (h_f), ft	16.5
Shear rate correction factor (C)	1	Turbulence parameter (C_{turb})	1.7
Salinity dependence slope (s_p)	0	Critical stress intensity factor (K_{IC}),, psi.inch$^{0.5}$	0
Carreau shear thinning index (n_1)	0.4		